Increasing Power Coefficient of Small Wind Turbine over a Wide Tip Speed Range by Determining Proper Design Tip Speed Ratio and Number of Blades

Oktay Yilmaz *

Yildiz Technical University, Faculty of Naval Architecture and Maritime, Marine Engineering Department, Istanbul 34349, Turkey

This manuscript has been published in *Proceedings of the Institution of Mechanical Engineers, Part C: Journal of Mechanical Engineering Science.*

Use the following link to access the paper's publisher version:

https://journals.sagepub.com/doi/10.1177/09544062221110396

To cite this paper:

Yilmaz O. *Increasing power coefficient of small wind turbine over a wide tip speed range by determining proper design tip speed ratio and number of blades.* Proceedings of the Institution of Mechanical Engineers, Part C: Journal of Mechanical Engineering Science. August 2022. DOI:10.1177/09544062221110396

* Corresponding author: E-mail: oktay@yildiz.edu.tr

Abstract

This paper proposes a design strategy based on an understanding of basic rotor aerodynamics principles to achieve aerodynamically efficient small wind turbine rotor by determining proper design tip speed ratio (TSR) and number of blades. In the design and performance analyses of rotors, the blade element momentum (BEM) method was employed in conjunction with the Viterna-Corrigan post-stall model and Buhl's wake state model. BEM simulations use the Re number dependent airfoil aerodynamic coefficients derived through Xfoil panel code. Reduced design tip speed ratio increased rotor solidity and hence blade Reynolds number. The width of the optimum TSR range, on the other hand, was found to decrease when the design TSR was less than a certain threshold. At high tip speeds, rotors with optimum design TSR were able to maintain an almost constant and near-ideal axial induction factor, resulting widest optimum TSR range for high aerodynamic efficiency. Increasing number of blades (B) increased $C_{P,max}$, but further increase in B lowered rotor efficiency due to reduced blade Re number. Based on CFD results, 5-blade SD7032 rotor with a design TSR of 4 achieved 12.3% higher $C_{P,max}$ compared to 0.9 m diameter 3-blade experimental reference rotor. Maximum achievable power coefficient of infinitely many-bladed ideal rotor with design TSR of 4 is 0.559, while $C_{P,max}$ of 5-blade SD7032 rotor is 0.492.

Keywords: Small wind turbine, aerodynamic efficiency, design tip speed ratio, number of blades, blade element momentum, axial induction factor, ideal rotor, Xfoil, computational fluid dynamics

Nomenclature

Abbreviations

BEM	Boundary Element Momentum
CFD	Computational Fluid Dynamics
LWT	Large Wind Turbine
SWT	Small Wind Turbine
VC	Viterna-Corrigan (model)

Latin Symbols

a,a'	axial and angular induction factor
AoA	angle of attack (°)
B	number of the blades
c	chord length (m)
C_l, C_d	lift and drag coefficient
$C_{l,design}$	design lift coefficient
C_P	power coefficient
D	rotor diameter (m)
F	tip loss factor
r,R	radial position and rotor radius (m)
R_{root}	blade root radius (m)
Re	Reynolds number
$\mathrm{Re_{tip}}$	tip Reynolds number
U_{rel}	relative wind velocity in the plane of rotation (m/s)
U_w	free stream wind speed (m/s)
$U_{w,design}$	design wind speed (m/s)

Greek Symbols

α	local angle of attack (°)
α_{design}	design angle of attack (°)
θ	section pitch angle (°)
λ	tip speed ratio
λ_{design}	design tip speed ratio
λ_r	local speed ratio of blade section
ν	kinematic viscosity (m^2/s)
φ	angle of relative wind (rad)
Ω	angular velocity of rotor (rad/s)

1. Introduction

A horizontal axis wind turbine (HAWT) with a rotor diameter of 8 m are considered small with reference to *International Electrotechnical Commission (IEC) 61400-2*.[1] Those with a rotor diameter of 1.25-3 m is included in the mini turbine subcategory, while 0.5-1.25 m is included in the micro turbine subcategory.[2] The total installed capacity of small wind turbines (SWTs) worldwide reached 1.8 GW as of 2020.[3]

SWTs are less efficient than large wind turbines (LWTs) because of their low blade Reynolds (Re) numbers. In addition, the cost of energy is higher for SWTs than for LWTs.[4] Capturing wind kinetic energy as much as possible is essential to reducing the energy costs of SWTs. While the aerodynamic power coefficient of modern LWTs is about 0.5 maximum, SWTs are below this level.[5] The maximum theoretical aerodynamic efficiency of wind turbines, referred to as the Betz limit, is 0.593.[6]

In terms of aerodynamic efficiency, the rotor design is the most important part of the designing process.[7] The chord and twist distribution, number of blades, design TSR, airfoil profile and wind speed affect rotor aerodynamic efficiency. Duquette et al.[8] studied the impact of rotor solidity on aerodynamic efficiency by scanning a wide range of solidity of 3, 6, and 12-blade rotors, with the maximum power coefficient standing as the primary performance measure. In the experiments, optimum performance of a 0.5-m diameter turbine was achieved with a 3-blade, low design TSR rotor. Sant et al.[9] reported on the design, installation, and power generation test results of a 9-blade turbine with a 3.4-m diameter to replace the American wind-driven water pump. The blades were shaped using the Eppler 197 airfoil profile. The design TSR, solidity, and maximum power coefficient of the multi-blade rotor designed by BEM were 3.2, 20.6%, and 0.45, respectively. They performed open field tests in a turbulent environment with an average wind speed of roughly 5 m/s and turbulence intensity more than 15%. Hitz and Wood[10] investigated several strategies and conducted numerical experiments to minimize the eccentricity of the rotor center of mass for a wind-driven water pump composed of 24 bent plates. They emphasized that the balancing operation is essential for vibration mitigation. Sarkis and Pinilla[11] conducted experimental work on 1/8 scale model rotor of a commercial wind-driven water pump. The S835 airfoil profile was used to shape 10-blade rotor, which had constant pitch angle and chord length. The rotor diameter, solidity, and design TSR were 300 mm, 69.2% and 1.2, respectively. The best performance was achieved at a pitch angle of 30°, with a power coefficient of 0.32. Wang and Chen[12] conducted a numerical study to investigate the effects of the blade number on the power and torque coefficients of a ducted turbine with a rotor diameter of 1.4 m. The performance of rotors with 2, 4, 6, and 8 blades with the same pitch angle or chord distribution was investigated.

Abdelwahed and Abd El-Rahman[7] derived a modified SG6043 airfoil by applying the genetic algorithm to maximize the lift-to-drag ratio. The authors employed Xfoil panel code[13] to generate aerodynamic coefficients of the airfoil. Increase in lift-to-drag ratio was achieved over a wide angle of attack (AoA) range at Re = 6×10^{4}. According to BEM simulations, if the modified SG6043 is preferred to the original SG6043 to shape the rotor blades of a 1.6 m diameter turbine, a 2% increase in maximum power coefficient can be achieved

and 5% more energy can be produced annually. Hsiao et al.[14] designed a 3-blade rotor shaped with NACA4418 airfoil for a 0.72 m diameter turbine. The authors employed Xfoil to generate Re number-dependent aerodynamic coefficients for BEM simulations. The maximum power coefficient of the turbine with a design TSR of 5 was 0.428.

Pourrajabian et al.[15] employed the optimization approach in conjunction with BEM theory to optimize the blade shapes of 0.5, 0.75 and 1 kW 3-blade SWTs to maximize the optimum power coefficient while reducing the rotor starting time. The authors revealed that a significant reduction in the turbine starting time can be achieved with a small reduction (1 to 2%) in the optimum power coefficient. The difference between the rotor with a short starting time and the optimum rotor provided by the BEM theory was larger chord length and pitch angle at the root. Hassanzadeh et al.[16] optimized the chord and twist distribution of a 2-blade turbine rotor with a 10 m diameter with the combination of BEM theory and optimization method. The rotor blades were shaped with S809 airfoil profile throughout. As a result of optimization, with reference to the original rotor, the chord lengths of the blade increased, and the twist angles were almost unchanged. Applying optimization technique embedded in BEM code, Sessarego and Wood[17] optimized the chord and twist distributions to maximize optimum power coefficient of 2.2 m diameter 3-blade turbines with aerodynamically efficient SG6043 and SD7062 airfoils. The maximum power coefficient of the SG6043 rotor was about 0.48, 2% higher than that of the SD7062 rotor.

Variable speed turbines operated with maximum power point tracking (MPPT) algorithm respond to changes in wind speed with a delay due to time lags in wind speed measurement[18], control system response time[19], and rotor inertia[20]. This causes the turbine to operate at a point less efficient than its maximum power coefficient.[21] Hence, high power coefficient in wide TSR range is highly desirable for efficient SWTs.[22] This way, the turbine will continue to produce energy with high aerodynamic efficiency at off-design operating points and will reach to the optimum rotation speed in a shorter time by getting high torque.

The blade sections of SWTs typically operate below Re = 5×10^5 where airfoil efficiency (lift-to-drag ratio) is strongly dependent on Re number.[23] Giguère and Selig[24] experimentally produced an extensive dataset of aerodynamic coefficients of 15 low Re number airfoils with a Re number range from 6×10^4 to 5×10^5. The authors pointed out that the blade Re number should not fall below 10^5, because most airfoil profiles have poor aerodynamic performance. Due to the high efficiency over a wide range of AoAs, Selig/Donovan SD70XX low Reynolds number airfoils[25] have been preferred to design new SWTs.[17,26]

The primary source of performance loss in SWTs is the low Reynolds number at blade sections. Much of the literature has focused on optimizing distribution of blade chord and twist for improved aerodynamic efficiency of 3-blade SWTs. However, improvement in aerodynamic efficiency remains limited in this way. The blade Reynolds number, on the other hand, is particularly sensitive to changes in the design tip speed ratio and the number of blades, both of which are important rotor design parameters. Nevertheless, wind-driven water pumps with multi-blade rotors, which are designed to produce high torque at low wind speeds

rather than generate power, received the greatest attention in the literature. There has been insufficient research into the aerodynamic efficiency of multi-blade SWTs used for power generation. Moreover, to the best of the author's knowledge, there is no systematic design methodology in the published literature that provides high power coefficient in the wide tip speed range of SWTs. This paper proposes a small wind turbine design methodology based on basic aerodynamic principles that does not require the use of advanced optimization methods while providing high power coefficient over wide tip speed range. This methodology achieves efficient multi-blade rotor design by undertaking a limited number of rotor design studies and performance analyses with comparatively low-cost numerical method blade element momentum. The second section introduces the BEM method, which considers Reynolds number dependent aerodynamic performance of rotor blades. The BEM approach and CFD simulations employed were verified by Krogstad and Lund's[23] experimental results of a 0.9 m diameter reference turbine, tested in a wind tunnel at the Norwegian University of Science and Technology. In the third section, the reasoning behind the effects of design TSR and number of blades on aerodynamic performance is discussed with a graphical interpretation. The BEM predictions of the two most efficient SD7032 rotors were tested by CFD simulations. The power coefficients of the designed optimum rotors and the reference rotor are given in comparison with ideal turbine power coefficients, which, unlike the Betz limit, are essentially dependent on the number of blades and design TSR. In the Conclusion Section, the introduced small wind turbine design methodology is summarized with its implications.

2. Method

2.1. BEM Method

The BEM method incorporates blade element theory and momentum theory into one.[18,27] The blade element theory requires lift and drag coefficients (C_l and C_d) of airfoils as a function of AoA to calculate forces acting on the rotor blade sections. On the other hand, the momentum theory applies conservation of linear and angular momentum on imaginary control volumes to determine local thrust and rotating forces. In BEM theory, the turbine rotor is divided into annular control volumes. The analytical expressions of thrust and torque obtained by the two methods of blade element and momentum theory are equated and the design/performance analysis equations are derived for wind turbine rotors. Two modifications were incorporated in the improved BEM method.[28] In generating post-stall aerodynamic coefficients of airfoils, Viterna-Corrigan (VC) Model[29] was employed. To achieve better numerical stability in the solution of rotor wake state, Buhl's method[30] was used.

2.1.1. Rotor design with BEM theory

A blade section with its geometric and flow parameters are depicted in Fig. 1. Incoming wind velocity (U_w), relative wind velocity in the plane of rotation (U_{rel}), axial induction factor (a), angular induction factor (a'),

angular velocity of the rotor (Ω), the radial position of the blade section (r), section pitch angle (θ), angle of attack (α), and angle of the relative wind (φ) are parameters in Fig. 1.

The design equations of Glauert optimum rotor are used and given below.[18] The distribution of φ was specified by,

$$\varphi = \frac{2}{3}\arctan\left(\frac{1}{\lambda_r}\right) \tag{1}$$

Here, the local speed ratio of the blade section $\lambda_r = \lambda_{design}\, r/R$. λ_{design} (= $\Omega R/U_w$) and R are the design TSR and the rotor radius, respectively. The chord distribution of the blades was specified by,

$$c = \frac{8\pi r}{BC_{l,design}}\left(1-\cos\varphi\right) \tag{2}$$

B and $C_{l,design}$ stand for number of blades, and design lift coefficient. The distribution of θ throughout the blade span was calculated by,

$$\theta = \varphi - \alpha_{design} \tag{3}$$

Here α_{design} is the design AoA. The rotor blade was divided into 25 sections. One of the output parameters of the design stage was the rotor solidity.

$$\sigma = \frac{B}{\pi R^2}\int_{R_{root}}^{R} c\,dr \cong \frac{B}{N\pi R}\sum_{i=1}^{N} c_i \tag{4}$$

Here i and N refer to the ith blade section and the number of blade sections respectively. R_{root} refers to the initial radial position of the true airfoil profile of the blades that captures wind energy. Comparison with experiments, setting of 20 for N was sufficient to obtain reliable results in BEM prediction for a 2.2 m diameter turbine.[31]

2.1.2 Aerodynamic performance prediction with BEM method

The methods 1 and 2 in the book of Manwell et al.[18] were utilized for aerodynamic analyses. The calculation procedure applied is as follows.

2.1.2.1 Method 1 (when a < 0.4)

1. The iteration process started with the initial estimate of the distributions of φ by use of Eq. (1).

2. The derivation procedure of BEM theory on page 125 in Manwell et al.[18] gives the following equation for C_l as a function of φ.

$$C_l = 4F\sin\varphi\,\frac{\cos\varphi - \lambda_r\sin\varphi}{\sigma_{local}\left(\sin\varphi + \lambda_r\cos\varphi\right)} \tag{5}$$

Here F and σ_{local} (= $Bc/2\pi r$) are the tip loss factor and the local blade solidity, respectively. F was calculated using Prandtl's method,

$$F = \frac{2}{\pi}\cos^{-1}\left[\exp\left(-\frac{B}{2\sin\varphi}\left(\frac{R}{r}-1\right)\right)\right] \tag{6}$$

C_l depending on angle of attack (α) for varying Re numbers was produced by Xfoil simulations (Fig. 3a).

$$C_l = \text{function of}\left(\alpha, \text{Re}\right) \quad \text{where } \alpha = \varphi - \theta \tag{7}$$

Reynolds number of blade sections is defined as $Re = U_{rel}\, c/\nu$, *where* $U_{rel} = U_w(1-a)/\sin\varphi$. The intersecting point (C_l corresponding to φ) of Eqs. (5) and (7) was numerically found for each blade section with the bisection root searching method in the interval of φ from 0° to 90°.

3. Once C_l and φ were determined, a and a' were calculated,

$$a = \left(1 + \frac{4F\sin^2\varphi}{\sigma_{local} C_l \cos\varphi}\right)^{-1} \tag{8}$$

$$a' = \frac{1}{2}\left(\sqrt{1+\frac{4}{\lambda_r^2}a(1-a)} - 1\right) \tag{9}$$

Equation (9) proposed by Lanzafame and Messina[32] was utilized for a'. Unlike the commonly used form in Manwell et al.[18] which is a function of both F and φ, Eq. (9) depends solely on a. This greatly simplified the numerical procedure in Method 2, as explained below.

4. Following the update of Re number, a new distribution of φ over the blade span was determined in step 2. The calculation procedure continued iteratively until convergence in φ was achieved.

2.1.2.2 Method 2 (when a > 0.4, wake state)

Method 2 was applied starting from the last blade section of Method 1 till the blade section at the tip.

1. As in Method 1, the iteration process started with the initial estimate of the distribution of φ.

2. When $a > 0.4$, Buhl[30] suggested Eq. (10) to eliminate numerical instability in BEM solution which appears when Glauert's correction is used.[32]

$$a = \frac{18F - 20 - 3\sqrt{C_{T_r}(50-36F)+12F(3F-4)}}{36F-50} \tag{10}$$

The relation for the local thrust coefficient (C_{Tr}) derived from BEM theory is given by (pg 131 in Manwell et al.[18]),

$$C_{T_r} = \frac{\sigma'(1-a)^2\left(C_l\cos\varphi + C_d\sin\varphi\right)}{\sin^2\varphi} \tag{11}$$

Utilizing the velocity triangle in Fig. 1, one can write the following relation between a, a', and φ.

$$\tan\varphi = \frac{1-a}{(1+a')\lambda_r} \tag{12}$$

Eqs. (6), (9)-(12) need to be solved. The fixed point iteration method is frequently employed in the literature.[28,31] In the fixed-point iteration, the equations are solved sequentially starting with the initial estimates of a and a' up to convergence. When Glauert correction was used, in some cases, the fixed point iteration algorithm converged to double roots that alternated between one and the other during subsequent iterations. Although adoption of Buhl's wake state model (Eq. 10) increased the number of solvable cases, convergence issues could not be completely eliminated. When the axial induction factor was relaxed using an under-relaxation factor of 0.5 in fixed-point iterations, most of the TSR values converged in BEM simulations performed for the Reference Rotor in Section 2.1.3. Despite attempting several values of relaxation factor, the algorithm diverged for a few TSR values. In the present study, Eqs. (9), (12), (6), (11), and (10) were substituted one into another sequentially to eliminate one parameter each time. By this way, Eq. (10) was reduced to a single parameter equation (as a function of axial induction factor, a). One-parameter Eq. (10) (not shown due to its complex form) was numerically solved with the bisection root searching method in the interval of a from 0.4 to 0.99.

3. After axial induction factor was determined in step 2, a', φ, F, and C_{Tr} were determined with Eqs. (9), (12), (6), and (11), respectively.

4. Steps 2 and 3 were repeated with updated values of C_d and C_l.

With the procedure outlined in Method 2, converged values of a were obtained in just two iterations. Finally, the power coefficient (C_P) was calculated for a specified λ.

$$C_P(\lambda) = \frac{8}{\lambda^2}\int_{\lambda_{root}}^{\lambda} F\lambda_r^3 a'(1-a)\left[1-\left(C_d/C_l\right)\cot\varphi\right]d\lambda_r \tag{13}$$

The BEM solution procedure was coded in Matlab environment (software version R2019a). Use of the bisection root finding algorithm completely eliminated convergence and numerical stability problems in methods 1 and 2. Song[33] reported that obtaining a convergent solution in BEM code was difficult around the stall AoA, and for negative AoAs (at high tip speeds).

2.1.3. Performance prediction of the Reference Rotor with BEM method

In this section, power coefficients predicted by BEM are compared with those of the experimental wind turbine in the work of Krogstad and Lund[23]. Rotor diameter (D) of the 3-blade turbine was 0.90 m. The rotor blade was shaped with S826 airfoil throughout the blade span. S826 airfoil, which is 14% thick of the chord, was specifically designed for HAWTs by National Renewable Energy Laboratory (NREL), USA.[34] The experiments were carried out within a closed return wind tunnel at the Norwegian University of Science and

Technology. The wind tunnel with 2.7 m by 2 m test cross-section had a free stream turbulence intensity of 0.3%. The experimental rotor considered for performance comparison purposes is hereinafter referred to as the Reference Rotor. The nonlinear chord and twist distributions of the rotor, and further details of the experimental work can be found in the mentioned literature.

The blockage ratio of the rotor, which is the rotor swept area divided by tunnel cross-section area, was 11.8%. Glauert's blockage correction[31,35] was applied to C_P and λ using reported values of the thrust coefficient (C_T) in Krogstad and Lund[23]. Experimental data with and without blockage correction are shown in Fig. 4. While C_P remains almost the same when λ is below 4, blockage effects become more obvious when λ is above 4.

In Xfoil simulations, the critical amplification factor (N_{crit}) was set to 3 to allow natural transition from laminar to turbulence[36] and 240 panel nodes were used around the airfoil profile. Figure 2 compares the aerodynamic coefficients of S826 airfoil, which were recently measured by Bartl et al.[37] after strenuous experimental efforts, with those estimated by Xfoil simulations. Xfoil predicted C_l and C_d fairly well throughout AoA range at Re = 100,000. Xfoil estimated optimistic values for moderate AoAs at Re = 50,000, though $C_{l,max}$ is lower than the experimental result. The tip Re number for almost all the rotors investigated, as shown in Tables 2 and 3, is about 100,000. The outer part of the rotor blade, with the highest local Re number, contributes the most to the generated power.[38] At low tip speeds, the rotor blade is operating at Re numbers less than 100,000 and stall AoAs as seen in Figs. 12b and 12c. It is known that rotational augmentation at stall angles of turbine blades improves aerodynamic efficiency of blade sections compared to 2D airfoil performance.[39] The centrifugal force generated by rotor rotation induces flow across the blade span, and the increased momentum of the boundary layer delays flow separation to higher AoAs.[40] The adoption of the Viterna-Corrigan Model for post-stall AoAs, as well as Xfoil's optimistic predictions at lower Re numbers, were considered useful in estimating rotational augmentation to some extent.[14] Aerodynamic coefficients were generated in Re number range of 0.2×10^5 to 5×10^5, this covers operating range of the rotors in Section 3.1. Viterna-Corrigan Model[41] was employed to generate airfoil coefficients from stall AoA to 90° (Fig. 3).

$$C_l = \frac{1}{2} C_{d,\max} \sin 2\alpha + K_l \frac{\cos^2 \alpha}{\sin \alpha} \tag{14}$$

$$C_d = C_{d,\max} \sin^2 \alpha + K_d \cos \alpha \tag{15}$$

The maximum drag coefficient, $C_{d,max}$, is determined by the following equation and corresponds to a 90° angle of attack.

$$C_{d,\max} = \begin{cases} 1.11 + 0.018AR & AR \le 50 \\ 2.01 & AR > 50 \end{cases} \tag{16}$$

The rotor blade aspect ratio (AR) equals the ratio of blade span to mean chord length. K_l and K_d in Eqs. (14) and (15) are given by,

$$K_l = \frac{\left(C_{l,stall} - C_{d,\max} \sin \alpha_{stall} \cos \alpha_{stall}\right) \sin \alpha_{stall}}{\cos^2 \alpha_{stall}} \tag{17}$$

$$K_d = \frac{\left(C_{d,stall} - C_{d,\max} \sin^2 \alpha_{stall}\right)}{\cos \alpha_{stall}} \tag{18}$$

Where $C_{l,stall}$ and $C_{d,stall}$ are the lift and drag coefficients at the stall AoA (α_{stall}).

Figure 4 depicts power coefficient predictions of the present BEM approach and those of BEM method applied by Krogstad and Lund[23]. The BEM model of Krogstad and Lund[23] and the present model have some similarities and differences. They also utilized Xfoil simulations to derive Re number dependent aerodynamic coefficients. They held to Xfoil's original predictions beyond the stall angle; no post-stall model was used. Their model included the Glauert correction for high induction cases and Prandtl's method for tip losses. BEM simulations of Krogstad and Lund[23] calculated C_P in reasonably good agreement with the experiments for TSR values less than 4, but considerably overestimated C_P above TSR = 4. Compared with experimental results corrected for blockage, the present BEM predictions showed a good match at rotor stalled state (small λ) and overestimated $C_{P,max}$ by 3.9%. In high tip speed range, decrease in C_P is steeper in the present BEM than in the experiments. The flow entrained from external stream to rotor wake near the blade tip provides a rise in wind speed outboard of the rotor blade.[42,43] In BEM method, stream tube passing through the rotor is isolated from external flow[18] and entrained flow is not taken into account, therefore axial induction factor near the tip region is overestimated. Because outer part of the blade contributes majority of the power produced at high tip speeds[38], it is considered that overestimating axial induction in the BEM method led to an underestimation of C_P. Along with many other 3D flow features, entrained flow from external wind stream can be predicted by CFD simulation of a fully resolved rotor. CFD and BEM simulations were used to generate C_P-λ curves of the two rotors with high design TSR, the Reference Rotor and SD7032-TSR6-B3, as are shown in Fig. 14a. At high tip speeds, the BEM method somewhat underestimated power coefficients of both rotors quite similarly. Following these considerations, the present BEM approach was deemed to be adequate in relative assessment of aerodynamic efficiency of newly designed rotors in Sections 3.1 and 3.2.

2.2. CFD prediction of the Reference Rotor performance

For the last few decades, CFD has been widely employed in wind turbine design and performance assessments, lowering the number of experiments needed for performance testing of various configurations.[44,45] k-ω SST turbulence model, a two-equation turbulence model from the family of Reynolds Averaged Navier-Stokes (RANS) models, gives a trade-off between computational accuracy and computation time. When compared to experimental data, k-ω SST model proved its success in predicting the boundary layer velocity profile for adverse pressure gradient separated flows.[46] Singh et al.[36] developed a new low Re number airfoil that operates between Re = 38,000 and 205,000 utilizing CFD simulations with the k-ω SST

turbulence model. The pressure distribution around the airfoil computed by CFD matched experimental data and Xfoil predictions fairly well. In their ongoing study, they achieved an increase in aerodynamic efficiency in open field tests with a two-blade 1.26 m-diameter turbine whose rotor was shaped with the new airfoil.[47] Koyuncuoğlu et al.[48] employed k-ω SST model in 2D and 3D CFD analyses to assess the aerodynamic characteristics of low Re number airfoils S826 and S809 at Re = 100,000. The lift and drag coefficients estimated by 2D CFD simulations agreed well with measurements up to stall AoA. Whereas 2D CFD did not produce consistent results in post-stall AoAs, 3D CFD analyses achieved very good accuracy. Numerous published research have successfully estimated the aerodynamic performance of SWTs with rotor diameters ranging from 0.7 to 1 m using k-ω SST turbulence model.[14,49-51]

In this study, RANS modelling was employed to solve governing equations of flow. The k-ω SST turbulence model was used to relate Reynolds stresses to time-averaged velocity gradients within the Boussinesq hypothesis.[52] CFD simulations were conducted using Ansys Fluent 19.2, which uses the finite volume method to discretize governing differential equations. Momentum equations in the moving reference frame, a cylindrical sub-computational domain (Figs. 5a and 5b) including the rotor, have additional terms of centripetal and Coriolis forces to account for the effects of rotor rotational motion on fluid flow.[52-54] With moving reference frame (MRF) approach, inherently unsteady flow around the turbine rotor was solved as a steady problem with respect to the non-inertial (moving) reference frame.[53] Flow was assumed to be incompressible, because Mach number of relative wind velocity for greatest TSR was just in compressibility limit even at the tip. The pressure-velocity coupling algorithm was used to simultaneously solve the momentum equations and the pressure-based continuity equation, giving solution with reduced iteration number. In spatial discretization, second order accurate upwind scheme was used for convective terms in continuity, momentum, k and ω equations. Gradients of variables were calculated by least squared cell-based method.

Rotor with its hub was included in the computational domain. Due to the periodicity of the turbine rotor, the governing equations were solved for just one third of the cylindrical computational domain (Fig. 5a).[51] Because the experimental results were corrected for blockage, CFD computations were performed in open field conditions with no wall effects. Following repeated CFD runs on 3R, 5R and 10R radius computational domains, it was seen that 1% blockage ratio (10R diameter) had a negligible effect on the calculated torque. The rotor was positioned 9R and 40R away from the inlet and outlet boundaries, respectively (Fig. 5b). The moving reference frame had a radius of 1.2R. Upstream and downstream planes of the moving reference frame were each 0.2R away from the rotating plane of the rotor. 10 m/s stream-wise velocity and 0.3% turbulence intensity were specified on the inlet boundary as in the experiments. Free slip wall boundary condition was applied at far field. Effective pressure at the outlet boundary was set to zero. The rotor's external surfaces were subjected to no-slip boundary condition.

A multi-block mesh was constructed in the computational domain to effectively control the mesh size. As shown in Fig. 5c, upstream zone and near wake region both extend a distance of 1R from the moving reference frame. Far wake region extends downstream 24R from the near wake region end. The mesh blocks of upstream zone, near wake, and far wake regions have a cylindrical shape with a radius of 1.67R. The effects of computational domain diameter, minimum-maximum face mesh sizes, rotor wake mesh density, first layer size, and total thickness of boundary layer mesh were investigated varying one parameter while fixing the remaining parameters. Computational domain diameter, first layer size, minimum face mesh size were the influential parameters on the computed torque and thrust. In addition, a mesh sensitivity analysis was carried out to ascertain the effects of overall mesh density and y^+ value. As seen in Table 1, the sensitivity of the torque to mesh density is much higher than that of the thrust. Torque calculated with Mesh C differs by less than 0.5% from that calculated with the highest mesh density, Mesh D. Mesh C, with a total of 3,470,885 mesh elements, consequently provided optimum density with y^+_{avg} = 0.8 and y^+_{max} = 4.2.

Table 1. Mesh sensitivity study results (the operating TSR of the rotor was 6).

	Number of mesh elements	y^+_{avg}	y^+_{max}	Torque (Nm)	Thrust (N)
Mesh A	1,389,843	23	74	1.116	30.15
Mesh B	1,932,754	4.4	18	1.200	31.10
Mesh C	3,470,885	0.8	4.2	1.275	31.68
Mesh D	6,563,223	0.2	0.95	1.272	31.65

This paragraph summarizes mesh sizing values of the optimum mesh as well as further details about the computational mesh structure. Upstream zone and near wake region were meshed with an element size of 50 mm. The mesh size was 100 mm in far wake region. Maximum mesh sizes in the moving reference frame and the entire computational domain were 25 and 200 mm, respectively. Initially, a triangular face mesh was created over the blade surface. The maximum and minimum face mesh sizes (in mm) in the root section, middle section and tip section were (1.6, 0.32), (1.25, 0.25) and (1.0, 0.2), respectively (Fig. 6). 20 layers of prismatic mesh elements with a growth rate of 1.25 were generated for the boundary layer mesh (Fig. 6d). The thickness of the first mesh element on the blade surface was 0.02 mm. An unstructured tetrahedral mesh was generated in Ansys Meshing for the entire computational domain, excluding prismatic mesh elements of the boundary layer. Then the tetrahedral mesh was transformed into polyhedral mesh in Ansys Fluent (Figs. 5c and 6). Blade face mesh was converted from triangular to the polygon. The minimum orthogonal quality of the mesh elements was around 0.32 and the maximum aspect ratio of the stretched boundary mesh over the blade surface was around 650.

The power coefficient was calculated by,

$$C_P = \frac{T\Omega}{0.5\rho A_{rotor} U_w^3} \tag{19}$$

Where T and A_{rotor} ($=\pi R^2$) are the rotor torque and rotor's swept area, respectively. The air density (ρ) was specified as 1.225 kg/m^3, which is the standard atmospheric value. Considering the entire λ range, CFD results matched the experimental results with blockage correction better than those without blockage correction (Fig. 4). CFD prediction is excellent in the stalled state (small λ range). The CFD results of Krogstad and Lund[23] are also displayed in Fig. 4. While their CFD results at low tip speeds matched the experiment, they highly overestimated C_P at TSR values beyond 4. To account for the blockage effect, they conducted rotor CFD simulations in a virtual wind tunnel with the same cross-sectional area as the experimental wind tunnel. The overestimation of the wake expansion diameter by CFD is believed to have constricted the external flow downstream of the turbine and forced more air to pass through the rotor than in the experiment, causing the power coefficient to be over predicted for high tip speeds.

3. Results and Discussion

3.1. Designing more efficient S826 rotor

Based on BEM theory, C_P of an ideal turbine without drag and tip losses is maximized by increase in B and λ_{design}. However, these two parameters are inversely proportional to each other for real turbines. B ranges from 1 to 3 for $\lambda_{design} > 4$, and 3 to 24 for $\lambda_{design} < 4$.[18] Modern LWT rotors are high tip speed machines with dominantly 3 blades. SWTs such as American windmill may have multi-blade rotors with low tip speeds. As λ_{design} increases, blade drag losses increase. On the other hand, as more blades are added, the wind turbine as a lift producing machine losses the benefit of high relative wind speed. Therefore, there should be optimum ranges of λ_{design} and B for better aerodynamic performance of SWTs.

Input design parameters for S826 rotors; $U_{w,design}$ = 10 m/s (the same as the Reference Rotor), α_{design} = 4.5^o, $C_{l,design}$ = 1.08, R = 0.45 m, and R_{root} = 0.0675 m. While these were fixed design parameters, λ_{design} and B were varying design parameters. S826 rotors are listed in Table 2 along with their solidity, Re_{tip} and $C_{P,max}$ values. Planforms of the Reference Rotor and S826 rotors are presented in Fig. 7. C_P data predicted by BEM is plotted in Fig. 8a. The change in the tip Re number depending on λ is depicted in Fig. 8b. Excluding lower tip speed range, the largest torque that contributed most to the power produced occurred around $r = 0.8R$. In this way, AoA and axial induction factor (a) at $r = 0.8R$ are displayed in Figs. 8c and 8d, respectively. An ideal turbine reaching the Betz limit (C_P = 0.593) has an axial induction factor equal to 1/3.[55] When a falls below this ideal value, the rotor behaves more permeable to the wind, and it converts less wind kinetic energy into rotational mechanical energy. When a approaches one, it behaves as a solid disc, allowing small amount of wind to flow through, reducing rotor efficiency.

Table 2. Solidity, Re_{tip}, $C_{P,max}$ and percent increase in $C_{P,max}$ with reference to the Reference Rotor.

Nr.	Rotor	λ_{design}	B	Solidity (%)	Re_{tip}	$C_{P,max}$	$\Delta C_{P,max}$ (%)
	Reference Rotor	6	3	8.44	1.00×10^5	0.429	-
1	S826-TSR5-B3	5	3	9.99	1.05×10^5	0.448	4.4
2	S826-TSR4-B3	4	3	14.35	1.30×10^5	0.439	2.3
3	S826-TSR3-B3	3	3	22.16	1.70×10^5	0.429	0.0
4	S826-TSR4-B4	4	4	14.35	1.00×10^5	0.454	5.8
5	S826-TSR3-B5	3	5	22.16	1.03×10^5	0.451	5.1
6	S826-TSR3.5-B4	3.5	4	17.64	1.10×10^5	0.444	3.5

Experience with the design equations (Eqs. (1)-(4)) showed that when the remaining design parameters, including B, were held constant, reducing λ_{design} resulted in an increase in solidity and operating Re number of blade sections (Refer to Fig. 8b for the change in Re number of the first three rotors designed). In this way, it was expected that blade sections operating with higher efficiency would provide higher rotor aerodynamic performance. For the first three S826 rotors illustrated in Figs.7b-d, λ_{design} was decreased from 5 to 3 while keeping B at 3. Solidity increased from 9.99% to 22.16%, while the tip Re number increased from 1.05×10^5 to 1.70×10^5. Compared with the Reference Rotor, S826-TSR5-B3 improved $C_{P,max}$ from 0.429 to 0.448 and increased the width of the optimum λ range (Fig. 8a). With S826-TSR4-B3, the optimum λ range widened even further. However, for S826-TSR3-B3 with the lowest λ_{design}, the width of the optimum λ range narrowed.

As λ_{design} decreased, AoA of the rotor blades became more sensitive to the change in λ (Fig. 8c). Moreover, for rotors with $\lambda_{design} = 3$, the axial induction factor has a downward trend in high tip speed range, indicating a reduction in wind energy capture (Fig. 8d). On the other hand, a for the high speed rotors (Reference Rotor and S826-TSR5-B3) increased dramatically, approaching 1 at the high λ range. At $\lambda = 10$, the increase of a for the rotors with $\lambda_{design} = 4$ was limited to 0.55. Due to moderate variation of AoA at low tip speeds and slight rise of a in high tip speeds, the optimum λ_{design} was 4, providing the widest optimum λ range (see C_P curve of S826-TSR4-B3 in Fig. 8a).

The increase in B attenuates the strength of tip vortices and, as a consequence, blade tip losses reduce.[55] Accordingly, for possible improvement in the fourth rotor design, λ_{design} was fixed at 4 and B was changed from 3 to 4 (Fig. 7e). Comparing with S826-TSR4-B3, $C_{P,max}$ of S826-TSR4-B4 raised from 0.448 to 0.454 and optimum λ range almost remained the same (Fig. 8a). Rotor solidity depends on λ_{design}, but not on B as seen in Table 2. However, increase in B decreases solidity per blade. The further increase in B while keeping λ_{design} at 4 caused Re_{tip} to fall below 10^5 where the airfoil efficiency rapidly deteriorates as seen in Fig. 3. For the fifth S826 rotor design, BEM simulations were carried out for S826-TSR3-B5 which maintained Re_{tip} around 10^5. $C_{P,max}$ of S826-TSR3-B5 is nearly the same as S826-TSR4-B4, however the optimum λ range is narrower. The negative impact of low λ_{design} on optimum λ range has already been discussed in this section. For the last rotor design, performance prediction was made for S826-TSR3.5-B4 which maintained more

uniformly distributed axial induction factor at high tip speeds (Fig. 8d). Nevertheless, S826-TSR4-B4 was considered the most energy efficient, as no further improvement in the optimum λ range could be achieved with the final rotor design, as seen in Fig. 8a. $C_{P,max}$ of S826-TSR4-B4 is 5.8% higher than that of the Reference Rotor (Table 2).

3.2. Designing more efficient SD7032 rotor

SD7032, a low Re number airfoil with 10% thickness of its chord, has some essential characteristics. Figure 9 compares the aerodynamic coefficients reported in Selig et al.[56] with those estimated by Xfoil simulations. Over the entire AoA range, from negative AoA to stall AoA, Xfoil predicted lift coefficient with good accuracy. The Xfoil and experimental results for the drag coefficient at Re = 100,000 showed good match, though Xfoil predictions for moderate AoAs at Re = 60,000 are somewhat optimistic. Figure 10 depicts the aerodynamic coefficients generated by combining Xfoil simulations and the VC model for varying Re number. SD7032's airfoil efficiency curves have relatively wide crests opposed to S826's spiky peaks (Fig. 10a). In addition, SD7032 efficiency exceeds S826 beyond 7° AoA. For Re = 50,000, SD7032 airfoil is more efficient over almost the entire AoA range.

The sole input design parameter that differed from S826 rotors was $C_{l,design}$ (0.894), which corresponded to α_{design} = 4.5° and Re = 10^5. SD7032 rotors designed are listed in Table 3 and presented in Fig. 11. C_P, Re_{tip}, AoA at $r = 0.8R$ and axial induction factor at $r = 0.8R$ depending on λ are depicted in Fig. 12. The first SD7032 rotor designed was SD7032-TSR5-B3 (Fig. 11b). The solidity of this rotor is 43% larger than that of the Reference Rotor. It raised Re_{tip} from 10^5 to 1.27×10^5. Furthermore, at high tip speeds, AoA of the rotor blades is less sensitive to the change in λ and the axial induction factor increases more slowly compared to the Reference Rotor (Figs. 12c and 12d). $C_{P,max}$ of SD7032-TSR-5-B3 is 5.3% higher. Its C_P is also greater through the entire λ range as seen in Fig. 12a.

Table 3. Solidity, Re_{tip}, $C_{P,max}$ and percent increase in $C_{P,max}$ with reference to the Reference Rotor.

Nr.	Rotor	λ_{design}	B	Solidity (%)	Re_{tip}	$C_{P,max}$	$\Delta C_{P,max}$ (%)
	Reference Rotor	6	3	8.44	1.00×10^5	0.429	-
1	SD7032-TSR5-B3	5	3	12.07	1.27×10^5	0.452	5.4
2	SD7032-TSR6-B3	6	3	8.85	1.06×10^5	0.453	5.6
3	SD7032-TSR4-B4	4	4	17.33	1.20×10^5	0.459	7.0
4	SD7032-TSR4-B5	4	5	17.33	0.95×10^5	0.467	8.9
5	SD7032-TSR3-B5	3	5	26.77	1.25×10^5	0.461	7.5
6	SD7032-TSR4-B7	4	7	17.33	0.65×10^5	0.468	9.1

For the second SD7032 rotor designed in Fig. 11c, B was fixed at 3 and, λ_{design} was set to 6 to take advantage of high relative wind speed. The AoA of this rotor blades is least sensitive to the change in λ (Fig. 12c). The rate of change of a with λ lies between that of the Reference Rotor and SD7032-TSR-5-B3 (Fig. 12d).

SD7032-TSR6-B3 is as aerodynamically efficient as SD7032-TSR5-B3 and, its solidity (8.85%) is almost the same as that (8.44%) of the Reference Rotor.

To see the effect of B, λ_{design} was fixed at 4, and B was set to 4 and 5 for the third and fourth rotors, respectively (Figs. 11d and 11e). In the high λ range, the two rotors were able to maintain an almost constant axial induction factor close to the ideal value (Fig. 12d). a was limited to 0.4 at its maximum. At the expense of the increase of solidity to 17.33%, $C_{P,max}$ of SD7032-TSR4-B5 is 8.9% higher than that of the Reference Rotor (Fig. 12a and Table 3). The fifth rotor depicted in Fig. 11f was SD7032-TSR3-B5, which substantially reduced the width of the optimum λ range. The last rotor designed was SD7032-TSR4-B7 (not illustrated in Fig. 11) which had the lowest Re_{tip} (0.65×10^5) due to decrease in solidity per blade (refer to Fig. 12b). As a result, the increase in B did not further improve $C_{P,max}$, but rather reduced C_P at high tip speeds (Fig. 12a). Because the drag coefficients around design AoA predicted by Xfoil at Re = 60,000 are smaller than the experiments, as shown in Fig. 9a, SD7032-TSR4-B7 must have a lower $C_{P,max}$.

SD7032-TSR4-B5 was the best performing rotor in terms of both $C_{P,max}$ and maintaining high aerodynamic efficiency across the widest range of λ. The aerodynamic efficiencies of the Reference Rotor, the most efficient rotor SD7032-TSR4-B5, and the low solidity rotor SD7032-TSR6-B3 are compared carrying out CFD simulations in the next section.

3.3. CFD prediction of performance of SD7032 rotors

CAD geometry of SD7032 rotors and the Reference Rotor are shown in Fig. 13. The CFD results and BEM predictions are presented in Fig. 14. The BEM predictions for SD7032 rotors are more in agreement with the CFD results than those for the Reference Rotor. CFD and BEM results showed good match at low tip speeds. More importantly, the CFD calculations showed improved aerodynamic efficiency achieved with SD7032 rotors, similar to the BEM predictions.

Figure 15a depicts C_P-λ curves predicted by CFD. $C_{P,max}$ of the Reference Rotor, SD7032-TSR6-B3 and SD7032-TSR4-B5 are 0.438, 0.465, and 0.492, respectively. MPPT algorithms ensure that variable speed turbines operate at optimum TSR (or at design TSR).[19] When the operating TSR of SD7032-TSR4-B5 rotor deviates from the design TSR to smaller tip speeds, its aerodynamic efficiency decreases markedly. At high wind speeds, operating TSR of variable speed turbines is small due to the maximum rotor speed limitation.[5] As a result, good aerodynamic efficiency at low tip speeds is essential in both constant and variable speed turbines in order to capture significant power potential of high speed winds.[57,58] Therefore, the anticipated operating TSR of SD7032-TSR4-B5 rotor was determined as 5 rather than the design TSR of 4 (Fig. 15a). The rotor's instantaneous TSR will fluctuate around the operating TSR in an urban setting due to turbulent wind. In terms of variable speed operation, SD7032-TSR4-B5 has a higher power coefficient than the Reference Rotor over almost the entire λ range. SD7032-TSR6-B3 rotor, on the other hand, offers highest aerodynamic

efficiency at high tip speeds. Conducting dynamic BEM simulations utilizing real-time wind speed data will be valuable for evaluating rotors based on energy harvesting performance in future studies.[21]

Figure 15b depicts the rotors' torque coefficients ($C_Q = Torque/0.5\rho\pi R^3U^2$) as a function of λ. 5-blade SD7032 rotor has substantially higher torque up to λ = 5 and delivers 2.5 and 3 times more starting torque compared to the Reference Rotor and 3-blade SD7032 rotor, respectively (see also Table 5).

It would be useful to compare $C_{P,max}$ values of the three rotors with maximum achievable power coefficient. The Betz limit is derived using the principle of conservation of linear momentum on the actuator disc and is independent of the number of blades and design TSR.[55] For a low speed rotor with small λ_{design}, the aerodynamic torque is large, due to the rotational wake velocity, less of the wind kinetic energy is converted into mechanical energy in the rotor, reducing aerodynamic efficiency. The Betz limit disregard the rotational kinetic energy left in the rotor wake. The wake rotation is taken into consideration when the angular momentum equation is applied to the actuator disc in conjunction with the linear momentum equation. The power coefficient of infinitely many-bladed ideal rotor as a function of λ_{design} is therefore calculated in this way (refer to Fig. 16).[18] The power coefficient of a three-blade ideal rotor was reported in the literature adopting BEM theory, taking into account wake rotation and ignoring drag and tip losses.[59] The $C_{P,max}$ of the Reference Rotor and SD7032-TSR6-B3 is 0.438 and 0.465, respectively, while the power coefficient of ideal 3-blade rotor is 0.536 for λ_{design} = 6 (the same as that of the two rotors), as seen in Table 4 and Fig. 16. While $C_{P,max}$ of SD7032-TSR4-B5 is 0.492, C_P of infinitely many-bladed ideal rotor is 0.559 for λ_{design} = 4. Low efficiency of low Re numbered blade sections is the major reason of SWT aerodynamic performance shortages.[60] While blade Re numbers of the small scale rotors in the present study are on the order of 10^5, those of MW size commercial turbines exceed 10^7. The particulars of the three rotors are given in Table 5.

Table 4. The three rotors' $C_{P,max}$ predicted by CFD, as well as the theoretical maximum C_P of ideal 3-blade and infinitely many-bladed rotors. C_P values of ideal rotor were received from the report of Wilson et al.[59]

	Maximum power coefficient ($C_{P,max}$)					
	Betz limit (no wake rotation)	Ideal rotor with infinite number of blades (with wake rotation)	3-blade ideal rotor (with wake rotation)	Reference Rotor (CFD)	SD7032-TSR6-B3 (CFD)	SD7032-TSR4-B5 (CFD)
λ_{design} = 4	0.593	0.559	0.509	n/a	n/a	0.492
λ_{design} = 6	0.593	0.574	0.536	0.438	0.465	n/a

As a final consideration, lift and drag coefficients at the Re_{tip} should be included in the aerodynamic data base for successful rotor design and accurate aerodynamic performance prediction using the BEM theory. The flow character is laminar over a portion of the airfoil surface at low Re number flows, with a laminar to turbulent flow transition occurring somewhere on the airfoil surface and a laminar separation bubble (LSB) may also

appear which impairs airfoil efficiency. The location of laminar-turbulent transition on airfoil surface, as well as whether LSB will occur, are determined by airfoil profile, surface roughness, AoA, Re number, and turbulence intensity in the free stream.[61,62] Xfoil predictions for S826 and SD7032 airfoils were in good agreement with the experimental data at the tip Re number of 100,000. Attempting to design smaller diameter rotors, on the other hand, will reduce Re_{tip}. As seen in this study, Xfoil predicted optimistic aerodynamic performance around Re = 50,000 for S826 and SD7032 airfoils. In this case, the BEM code using Xfoil aerodynamic data will overestimate C_P. In this respect, it is very important to experimentally produce aerodynamic coefficients at lower Re numbers within the scope of smaller scale wind turbine design and performance analysis.[60]

Table 5. Particulars of the rotors (D = 0.9 m).

		Reference Rotor	SD7032-TSR6-B3	SD7032-TSR4-B5
Tip pitch angle	$Ø_{tip}$ (deg)	-0.7	1.8	4.9
Root pitch angle	$Ø_{root}$ (deg)	37.1	27.5	34.9
Tip chord length	c_{tip} (cm)	2.6	2.6	3.4
Root chord length	c_{root} (cm)	8.1	9.6	8.6
Rotor solidity	σ (%)	8.44	8.85	17.33
Tip Re number	Re_{tip}	1.05×10^5	1.06×10^5	0.95×10^5
Starting torque *	$T_{\lambda=0}$ (Nm)	0.219	0.174	0.522
Max. power coeff. *	$C_{P,max}$	0.438	0.465	0.492

* These parameters are based on CFD results and correspond to $U_{w,\ design}$.

4. Conclusions

Experience gained with the BEM method for designing small wind turbines with high power coefficient in a wide TSR range is summarized below.

1. Based on the BEM design equations, lowering the design tip speed ratio increased rotor solidity and hence blade Reynolds number. However, width of the optimum TSR range was found to decrease when the design TSR was below a limit value. Indeed, when operating TSR deviated from the design TSR, more severe change occurred in blade AoA of low speed rotors, resulting in reduced aerodynamic efficiency. The sensitivity of AoA of rotor blades to change in TSR was particularly sensitive at low tip speeds. Moreover, when the design TSR was smaller than the optimum design TSR, axial induction factor dropped below the ideal value (1/3) at high tip speeds, indicating that rotor was capturing less wind energy. When the design TSR was higher than the optimum design TSR, axial induction factor increased dramatically at high tip speeds, signifying that the rotor resisted wind, resulting in reduced flow across the rotor. Rotors with optimum design TSR provided an almost constant and near-ideal axial induction factor at high tip speeds. For S826 and SD7032 rotors, the optimum design TSR was 3.5-4 and 4, respectively, providing the widest optimum TSR range.

2. For fixed design TSR, increase in number of blades (B) led to increase in $C_{P,max}$. When the design TSR is held constant, the rotor solidity remains unchanged as B increases, but the solidity per blade decreases.

Therefore, increase in B was limited due to concerns about low blade Re numbers. After determining the optimum design TSR in step 1, B was gradually increased to find the rotor with the highest $C_{P,max}$.

Based on an understanding of basic rotor aerodynamics principles, it is possible to considerably increase the aerodynamic efficiency of a SWT rotor by performing a small number of BEM design studies and subsequent BEM performance analyses.

For effective rotor design and performance prediction utilizing BEM simulations, lift and drag coefficients at the tip Re number must be provided. It is not a major concern that Xfoil overestimated aerodynamic efficiency to some extent from experimental results around Re = 50,000, since such low Re numbers were encountered at low tip speeds where the blade stalls owing to large AoAs. As is known from the published literature, at stall angles, centrifugal pumping, or in other words rotational augmentation, improves the aerodynamic efficiency of blade sections relative to 2D airfoil efficiency. In performance analysis of SWTs, Viterna-Corrigan model was used to derive the aerodynamic coefficients in post-stall AoAs. The BEM predictions agreed well with the experiments and CFD results in the blade stall state of low tip speeds.

Based on CFD simulation results, 3-blade SD7032 rotor with a design TSR of 6 and 5-blade SD7032 rotor with a design TSR of 4 achieved 6.2% and 12.3% greater $C_{P,max}$ than the Reference Rotor (0.9 m diameter 3-blade S826 rotor), respectively. Throughout the operating TSR range, both 3-blade and 5-blade SD7032 rotors have a higher power coefficient than the Reference Rotor. Further, as compared to the Reference Rotor, 5-blade SD7032 rotor delivers 2.5 times more starting torque. Because of the finite number of blades and the rotation wake behind the turbines, maximum power coefficient that an ideal turbine can achieve is less than the Betz limit (0.593). $C_{P,max}$ values of the rotors were compared to the ideal turbine power coefficients available in literature, which vary depending on the design TSR and number of blades. While $C_{P,max}$ of SD7032-TSR4-B5 is 0.492, power coefficient of infinitely many-bladed ideal rotor is 0.559 for $\lambda_{design} = 4$.

In this work, the design equations of Glauert optimum rotor were used. Following the determination of the optimum design tip speed ratio and number of blades, aerodynamic efficiency can possibly be improved to some degree by optimizing the chord and pitch distribution using advanced optimization methods such as genetic algorithm.

Acknowledgements

The author would also like to appreciate Yildiz Technical University for the licence support of Matlab and Ansys Fluent softwares.

Declaration of conflicting interests

The Author declares that there is no conflict of interest

Funding

This research received no specific grant from any funding agency in the public, commercial, or not-for-profit sectors.

References

1. IEC 61400-2:2006. Wind turbines. Design requirements for small turbines.
2. Tummala A, Velamati RK, Sinha DK, et al. A review on small scale wind turbines. *Renew Sustain Energy Rev* 2016; 56: 1351–1371.
3. U.S. Department of Energy. 2021 distributed wind market report, https://www.energy.gov/eere/wind/articles/distributed-wind-market-report-2021-edition-released (2021, accessed 13 May 2022).
4. Pagnini LC, Burlando M, Repetto MP. Experimental power curve of small-size wind turbines in turbulent urban environment. *Appl Energy* 2015; 154: 112–121.
5. Wood D. *Small wind turbines*. 1st ed. London: Springer, 2011.
6. Burton T, Jenkins N, Sharpe D, et al. *Wind energy handbook*. 2nd ed. Chichester: John Wiley & Sons, 2011.
7. Abdelwahed KS, Abd El-Rahman AI. Shape optimization of SG6043 airfoil for small wind turbine blades. *J Phys Conf Ser* 2020; 1618: 042007.
8. Duquette MM, Swanson J, Visser KD. Solidity and blade number effects on a fixed pitch, 50W horizontal axis wind turbine. *Wind Eng* 2003; 27: 299–316.
9. Sant T, Farrugia RN, Muscat M, et al. Development and performance testing of a small, multi-bladed wind turbine. *Wind Eng* 2020; 44: 3–20.
10. Hitz K, Wood D. On blade arrangement for multi-blade rotors. *Wind Eng* 2011; 35: 329–338.
11. Sarkis N, Pinilla AE. Experimental study on a model of a commercial windpumping rotor. *Wind Eng* 2006; 30: 511–520.
12. Wang SH, Chen SH. Blade number effect for a ducted wind turbine. *J Mech Sci Technol* 2008; 22: 1984–1992.
13. Drela M. XFOIL: An analysis and design system for low Reynolds number airfoils. In: Mueller TJ (eds) *Low Reynolds number aerodynamics. Lecture notes in engineering*. Berlin: Springer, 1989, pp.1–12.
14. Hsiao F Bin, Bai CJ, Chong WT. The performance test of three different horizontal axis wind turbine (HAWT) blade shapes using experimental and numerical methods. *Energies* 2013; 6: 2784–2803.
15. Pourrajabian A, Ebrahimi R, Mirzaei M. Applying micro scales of horizontal axis wind turbines for operation in low wind speed regions. *Energy Convers Manag* 2014; 87: 119–127.
16. Hassanzadeh A, Hassanzadeh Hassanabad A, Dadvand A. Aerodynamic shape optimization and analysis of small wind turbine blades employing the Viterna approach for post-stall region. *Alexandria Eng J* 2016; 55: 2035–2043.

17. Sessarego M, Wood D. Multi-dimensional optimization of small wind turbine blades. *Renewables Wind Water, Sol* 2015; 2: 9.
18. Manwell JF, McGowan JG, Rogers AL. *Wind energy explained: Theory, design and application*. 3rd ed. Chichester, John Wiley & Sons, Ltd, 2009.
19. Tang C, Pathmanathan M, Soong WL, et al. Effects of inertia on dynamic performance of wind turbines. In: *2008 Australasian Universities Power Engineering Conference*, Sydney, Australia, 14-17 December 2008, paper no. P-087, pp. 1–6. New Jersey: IEEE.
20. Battisti L, Benini E, Brighenti A, et al. Small wind turbine effectiveness in the urban environment. *Renew Energy* 2018; 129: 102–113.
21. Tang C, Soong WL, Freere P, et al. Dynamic wind turbine output power reduction under varying wind speed conditions due to inertia. *Wind Energy* 2013; 16: 561–573.
22. Salgado V, Troya C, Moreno G, et al. Airfoil selection methodology for small wind turbines. *Int J Renew Energy Res* 2016; 6: 1410–1415.
23. Krogstad P-Å, Lund JA. An experimental and numerical study of the performance of a model turbine. *Wind Energy* 2012; 15: 443–457.
24. Giguère P, Selig MS. Low Reynolds number airfoils for small horizontal axis wind turbines. *Wind Eng* 1997; 21: 367–380.
25. Selig, Donovan, Fraser. *Airfoils at low speeds*. 1st ed.Virginia, H. A. Stokely, 1989.
26. Matsumiya H, Ito R, Kawakami M, et al. Field operation and track tests of 1-kW small wind turbine under high wind conditions. *J Sol Energy Eng* 2010; 132: 0110021–0110028.
27. Rachman A, Johnstone A, Kosasih B. The effects of shape and size on duct-augmented horizontal axis turbine performance. *Wind Eng* 2021; 45: 953–972.
28. Song Q, Lubitz WD. BEM simulation and performance analysis of a small wind turbine rotor. *Wind Eng* 2013; 37: 381–399.
29. Viterna LA and Corrigan RD. Fixed pitch rotor performance of large horizontal axis wind turbines. Report, NASA Lewis Research Center, USA, January 1982.
30. Buhl ML. A new empirical relationship between thrust coefficient and induction factor for the turbulent windmill state. Report NREL/TP-500-36834, National Renewable Energy Laboratory, USA, August 2005.
31. Refan M, Hangan H. Aerodynamic performance of a small horizontal axis wind turbine. *J Sol Energy Eng Trans ASME* 2012; 134: 1–7.
32. Lanzafame R, Messina M. Fluid dynamics wind turbine design: Critical analysis, optimization and application of BEM theory. *Renew Energy* 2007; 32: 2291–2305.
33. Song Q. *Design, fabrication, and testing of a new small wind turbine blade*. Master's Thesis, University of Guelph, Canada, 2012.
34. Somers D. The S825 and S826 airfoils. Report NREL/SR-500-36344, National Renewable Energy Laboratory, USA, January 2005.

35. Bahaj AS, Molland AF, Chaplin JR, et al. Power and thrust measurements of marine current turbines under various hydrodynamic flow conditions in a cavitation tunnel and a towing tank. *Renew Energy* 2007; 32: 407–426.
36. Singh RK, Ahmed MR, Zullah MA, et al. Design of a low Reynolds number airfoil for small horizontal axis wind turbines. *Renew Energy* 2012; 42: 66–76.
37. Bartl J, Sagmo KF, Bracchi T, et al. Performance of the NREL S826 airfoil at low to moderate Reynolds numbers—A reference experiment for CFD models. *Eur J Mech B/Fluids* 2019; 75: 180–192.
38. Wood DH. Dual purpose design of small wind turbine blades. *Wind Eng* 2004; 28: 511–528.
39. Sicot C, Devinant P, Loyer S, et al. Rotational and turbulence effects on a wind turbine blade. Investigation of the stall mechanisms. *J Wind Eng Ind Aerodyn* 2008; 96: 1320–1331.
40. Thumthae C, Chitsomboon T. Improved 3D stall delay model for wind turbine design. *12th Am Conf Wind Eng 2013, ACWE 2013 Wind Eff Struct Communities, Energy Gener* 2013; 2: 1080–1089.
41. Martínez J, Bernabini L, Probst O, et al. An improved BEM model for the power curve prediction of stall-regulated wind turbines. *Wind Energy* 2005; 8: 385–402.
42. Jamieson PM. Beating betz: Energy extraction limits in a constrained flow field. *J Sol Energy Eng Trans ASME* 2009; 131: 0310081–0310086.
43. Johansen J, Madsen HA, Gaunaa M, et al. Design of a wind turbine rotor for maximum aerodynamic efficiency. *Wind Energy* 2009; 12: 261–273.
44. González Madina F, Gutiérrez A, Galione P. Computational fluid dynamics study of Savonius rotors using OpenFOAM. *Wind Eng* 2021; 45: 630–647.
45. Major D, Palacios J, Maughmer M, et al. Aerodynamics of leading-edge protection tapes for wind turbine blades. *Wind Eng* 2021; 45: 1296–1316.
46. Menter FR. Improved two-equation k-omega turbulence models for aerodynamic flows. Report, NASA Ames Research Center, USA, October 1992.
47. Singh RK, Ahmed MR. Blade design and performance testing of a small wind turbine rotor for low wind speed applications. *Renew Energy* 2013; 50: 812–819.
48. Koyuncuoğlu AC, Yilmaz O, Oğuş MÜ. Numerical investigation of aerodynamic characteristics of low Reynolds number airfoils S826 and S809. In: *International Eurasian Conference on Science, Engineering and Technology,* Ankara, Turkey, 22-23 November 2018, pp. 2276–2284.
49. Shives M, Crawford C. Developing an empirical model for ducted tidal turbine performance using numerical simulation results. *Proc Inst Mech Eng Part A J Power Energy* 2012; 226: 112–125.
50. Lipian M, Dobrev I, Massouh F, et al. Small wind turbine augmentation: Numerical investigations of shrouded- and twin-rotor wind turbines. *Energy* 2020; 201: 117588.
51. Khalafallah MG, Ahmed AM, Emam MK. CFD study of some factors affecting performance of HAWT with swept blades. *Int J Sustain Energy* 2017; 36: 489–501.
52. Ansys Fluent Theory Guide 19.2, 2019.

53. Silva PASF, Rio Vaz DATD, Britto V, et al. A new approach for the design of diffuser-augmented hydro turbines using the blade element momentum. *Energy Convers Manag* 2018; 165: 801–814.
54. Potsdam M, Mavriplis D. Unstructured mesh CFD aerodynamic analysis of the NREL Phase VI rotor. In: *47th AIAA Aerospace Sciences Meeting including The New Horizons Forum and Aerospace Exposition*, Orlando, Florida, 5-8 January 2009, paper no. 1221, pp. 1–18.
55. Hansen M. *Aerodynamics of wind turbines*. 3rd ed. London and Newyork: Routledge, 2015.
56. Selig MS, Guglielmo JJ, Broeren AP, et al. *Summary of low-speed airfoil data*. 1st ed. Virginia: Soartech Publications, 1995.
57. Lanzafame R, Messina M. Power curve control in micro wind turbine design. *Energy* 2010; 35: 556–561.
58. Song Q, David Lubitz W. Design and testing of a new small wind turbine blade. *J Sol Energy Eng Trans ASME* 2014; 136: 5–8.
59. Wilson RE, Lissaman PBS and Walker SN. Aerodynamic performance of wind turbines. Report, Oregon State University, USA, June 1976.
60. Van Treuren KW. Small-scale wind turbine testing in wind tunnels under low Reynolds number conditions. *J Energy Resour Technol Trans ASME* 2015; 137: 1–11.
61. Shyy W, Lian Y, Tang J, et al. *Aerodynamics of low Reynolds number flyers*. 1st ed. Cambridge: Cambridge University Press, 2008.
62. Genç MS, Karasu İ, Açıkel HH, et al. Low Reynolds number flows and transition. In: Genç MS (eds) *Low Reynolds number aerodynamics and transition*. Rijeka: InTech, 2012, pp. 3–28.

Figure Captions

Fig. 1. Geometric and flow parameters of a blade section.

Fig. 2. Comparison of the aerodynamic coefficients of S826 airfoil predicted by Xfoil with experimental data.

Fig. 3. Lift and drag coefficients of S826 predicted by Xfoil and extended beyond stall AoA by VC Model.

Fig. 4. Power coefficient of the Reference Rotor as a function λ at a free stream wind speed (U_w) of 10 m/s. Experimental data without blockage correction was reported in Krogstad and Lund[23].

Fig. 5. a) 3D view of computational domain. For clarity, only periodic planes, outlet, moving reference frame, and rotor blade are shown. b) Boundary conditions and sizes of the computational domain (not to scale). c) Mesh structure on one of the periodic planes, borders and sizes of mesh refinement zones.

Fig. 6. The blade surface mesh a) tip section, b) middle section, c) root section. d) Boundary layer meshes at the tip section.

Fig. 7. The Reference Rotor and S826 rotors designed. (TSR and B represent λ_{design} and number of blades in naming the rotors).

Fig. 8. a) Power coefficient, b) tip Re number, c) AoA at $r = 0.8R$ and, d) axial induction factor (a) at $r = 0.8R$ as a function of the tip speed ratio. Solid circles on the curves indicate the design TSR of the rotors.

Fig. 9. Comparison of the aerodynamic coefficients of SD7032 predicted by Xfoil with experimental data.

Fig. 10. a) Airfoil efficiency, b) lift, and c) drag coefficients predicted by Xfoil and VC model.

Fig. 11. The Reference Rotor and SD7032 rotors designed.

Fig. 12. a) Power coefficient, b) tip Re number, c) AoA at $r = 0.8R$ and, d) axial induction factor (a) at $r = 0.8R$ as a function of the tip speed ratio. Solid circles on the curves indicate the design TSR of the rotors.

Fig. 13. CAD geometry of selected rotors. Reference Rotor was reproduced from Krogstad and Lund[23].

Fig. 14. Comparison of BEM predictions with CFD results a) SD7032-TSR6-B3, and b) SD7032-TSR4-B5.

Fig. 15. a) Power coefficients of the rotors (CFD results). SD7032-TSR4-B5's x-axis is shifted one λ to the right. The solid circles on the curves show the design TSR. b) Torque coefficients of the rotors (CFD results).

Fig. 16. The three rotors' $C_{P,max}$ predicted by CFD, as well as the theoretical maximum C_P of ideal 3-blade and infinitely many-bladed rotors. C_P curves of ideal rotors are reported in Wilson et al.[59]

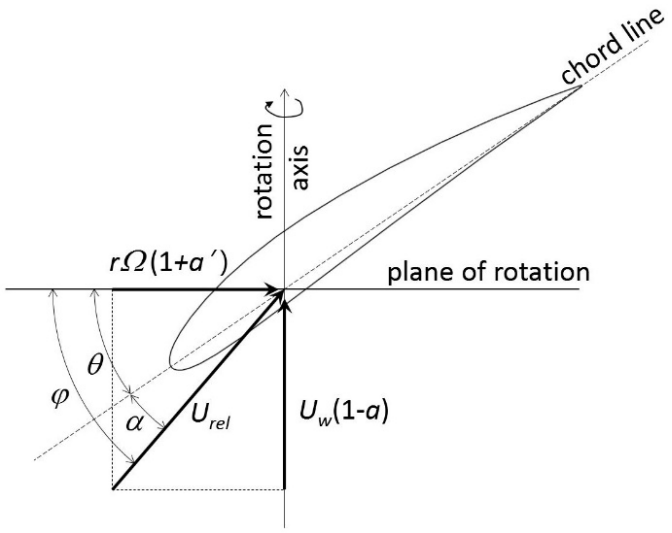

Fig. 1. Geometric and flow parameters of a blade section.

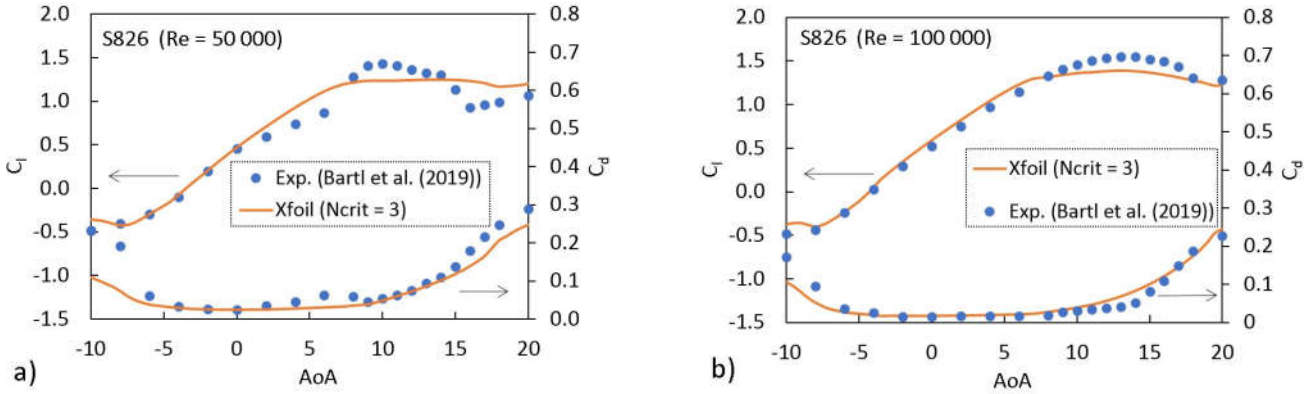

Fig. 2. Comparison of the aerodynamic coefficients of S826 airfoil predicted by Xfoil with experimental data.

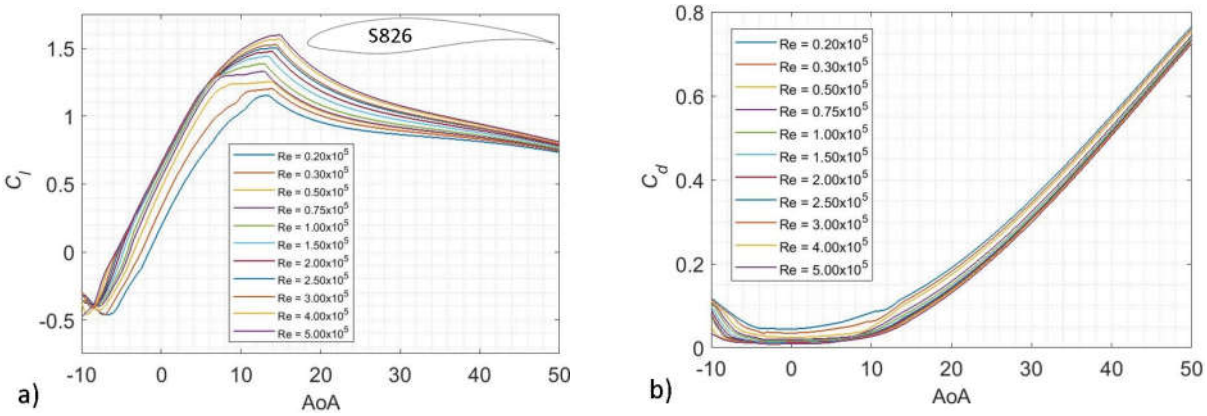

Fig. 3. Lift and drag coefficients of S826 predicted by Xfoil and extended beyond stall AoA by VC Model.

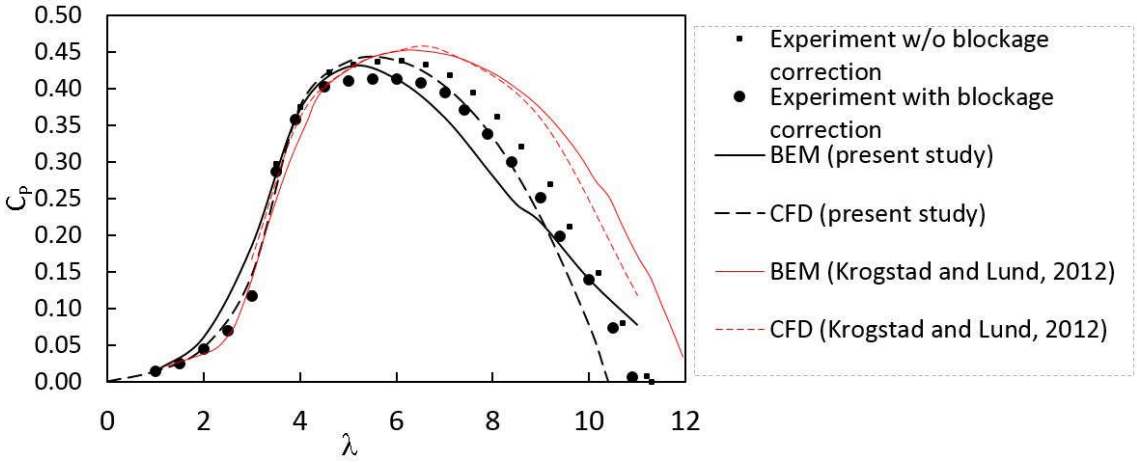

Fig. 4. Power coefficient of the Reference Rotor as a function λ at a free stream wind speed (U_w) of 10 m/s. Experimental data without blockage correction was reported in Krogstad and Lund[23].

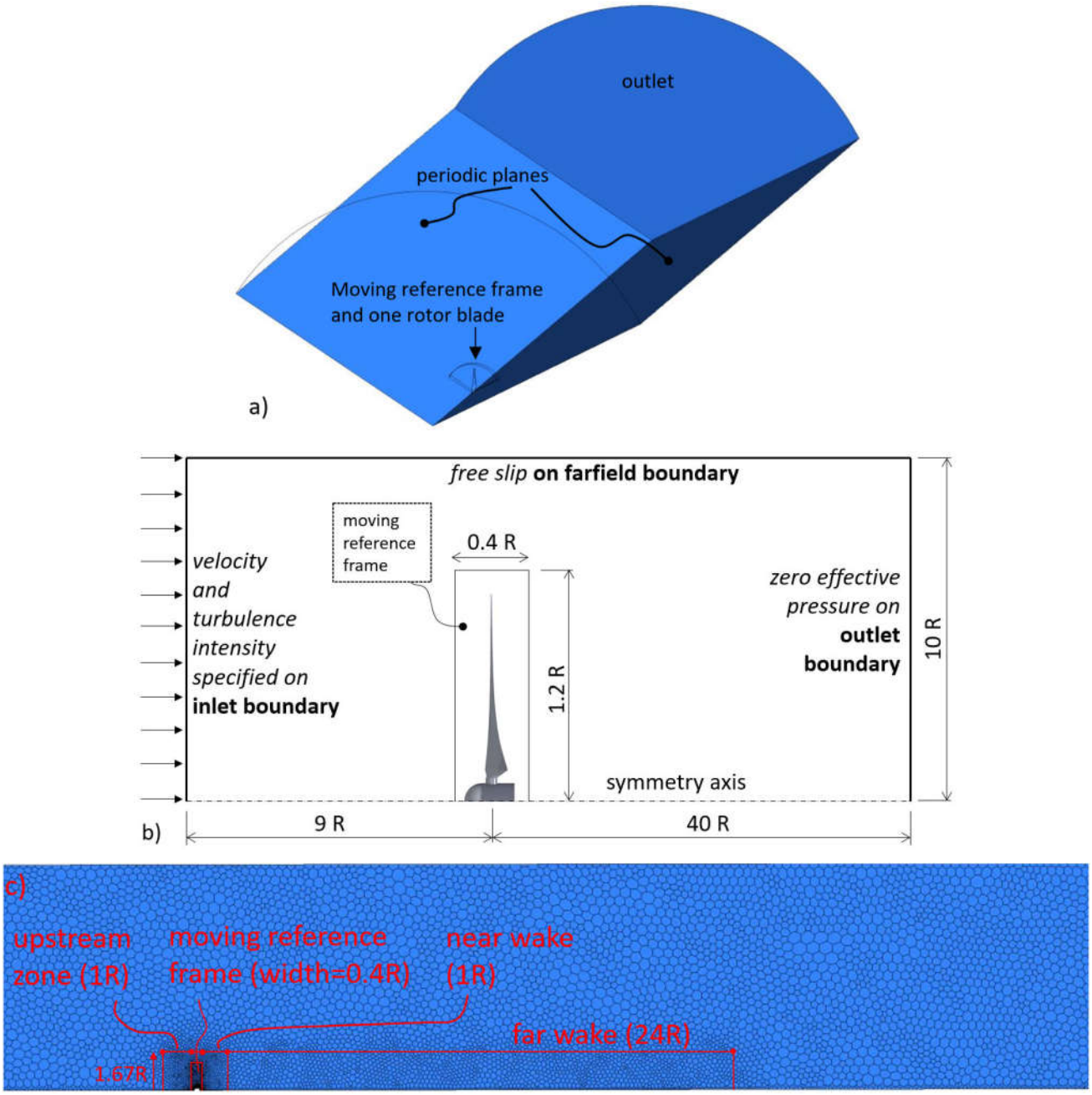

Fig. 5. a) 3D view of computational domain. For clarity, only periodic planes, outlet, moving reference frame, and rotor blade are shown. b) Boundary conditions and sizes of the computational domain (not to scale). c) Mesh structure on one of the periodic planes, borders and sizes of mesh refinement zones.

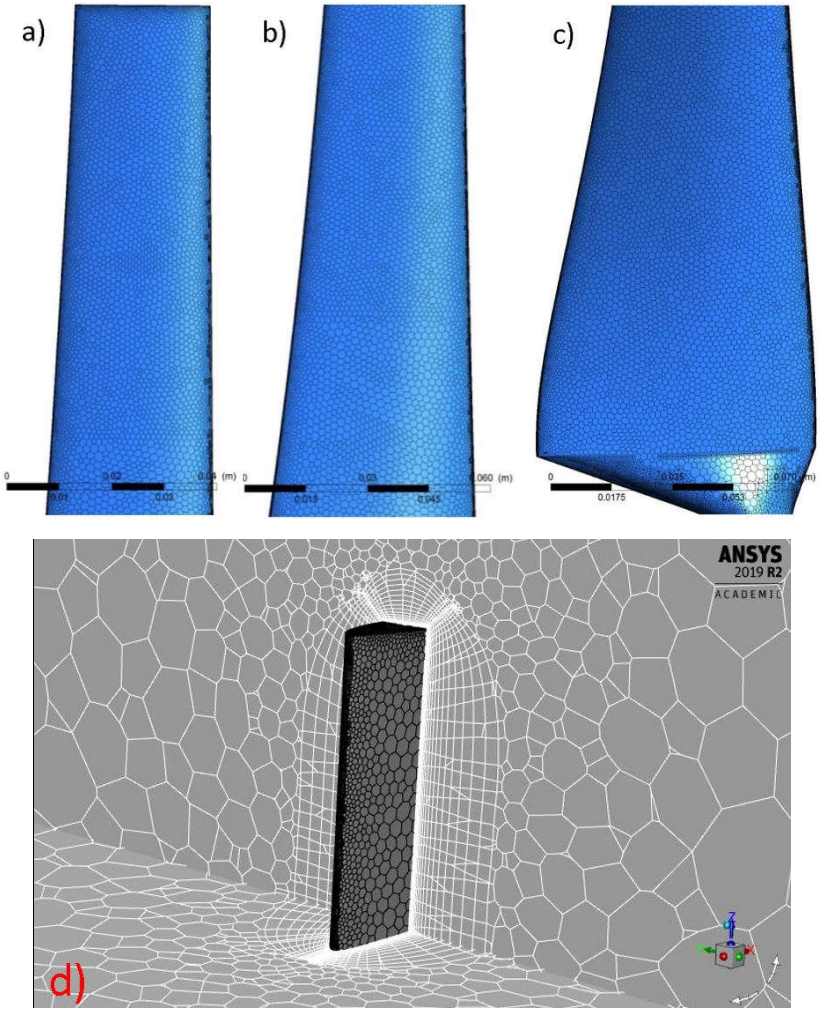

Fig. 6. The blade surface mesh a) tip section, b) middle section, c) root section. d) Boundary layer meshes at the tip section.

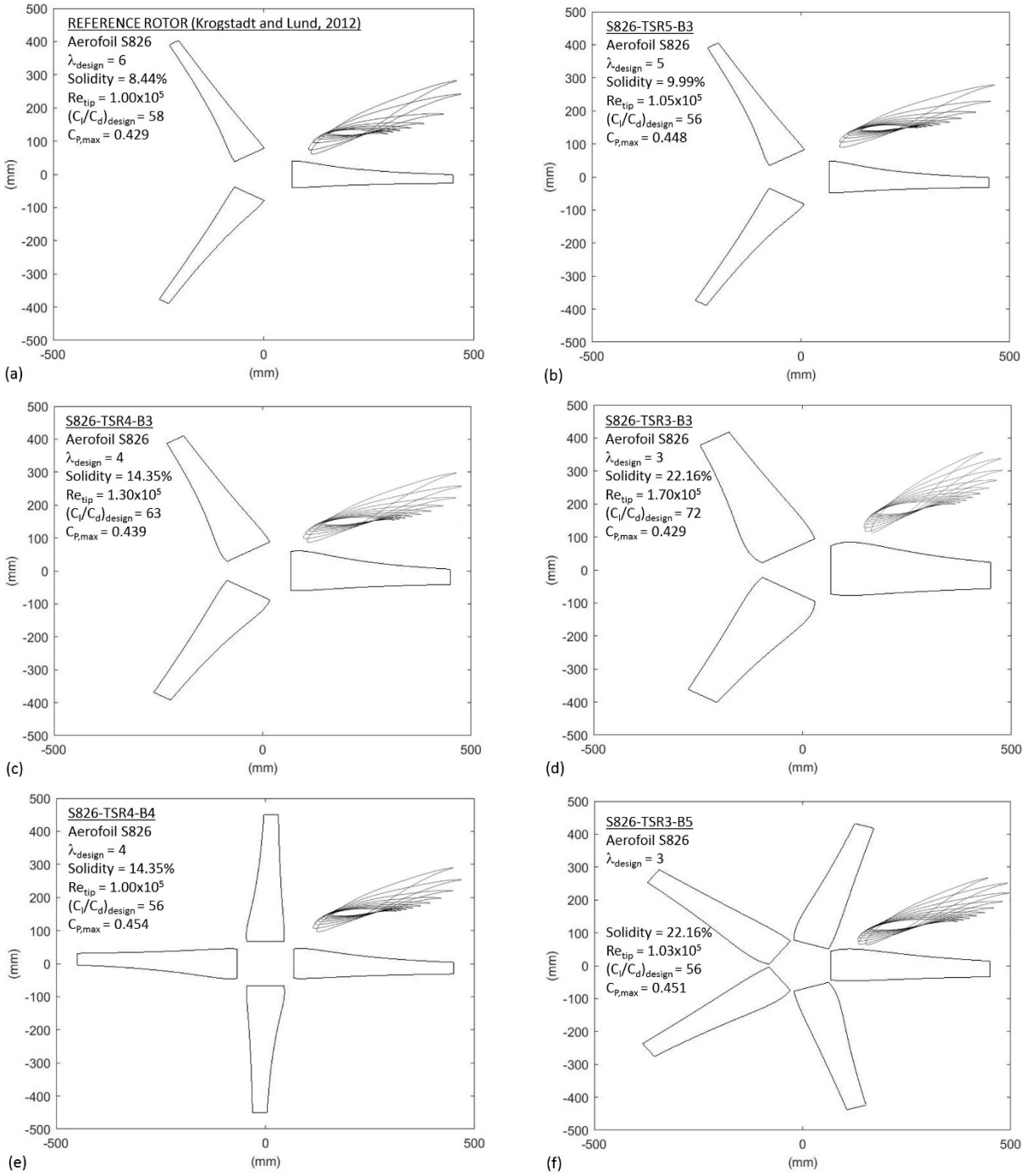

Fig. 7. The Reference Rotor and S826 rotors designed. (TSR and B represent λ_{design} and number of blades in naming the rotors).

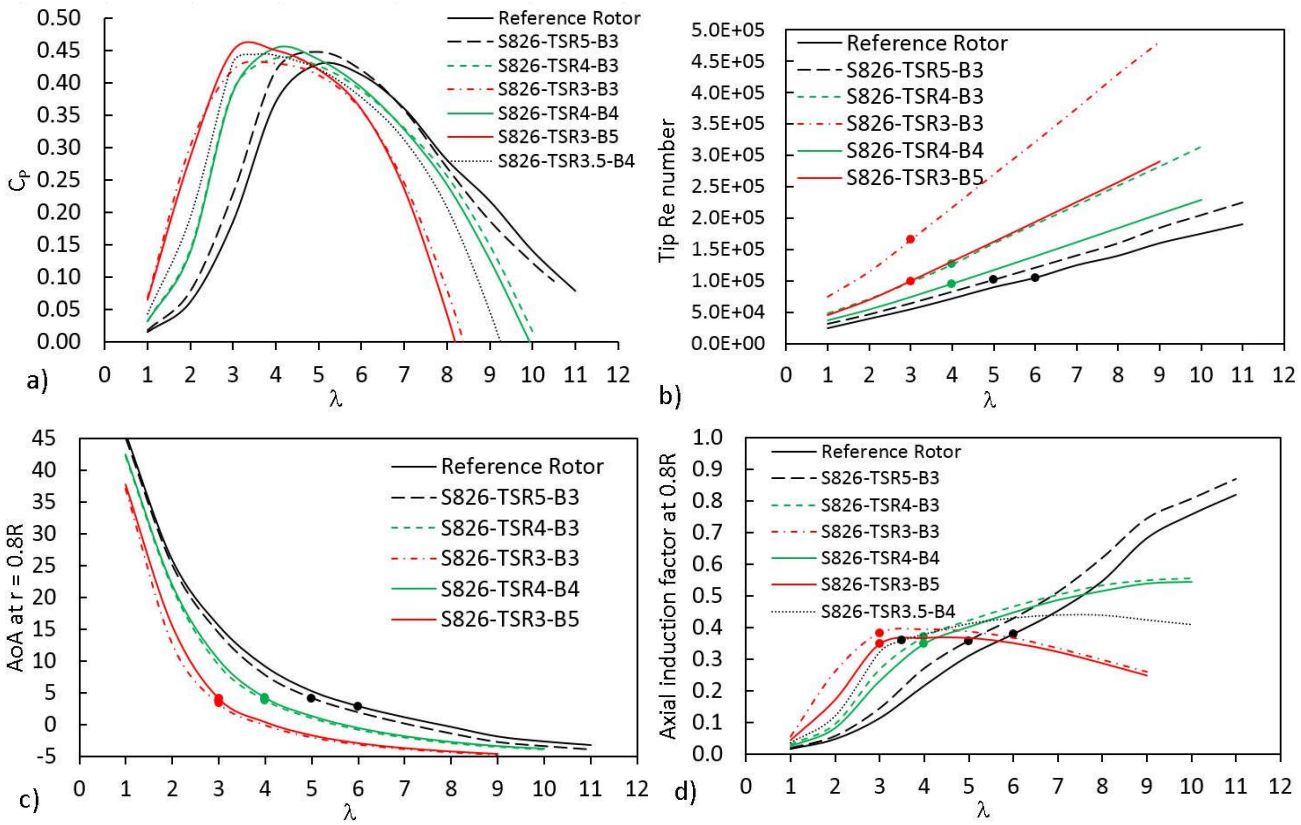

Fig. 8. a) Power coefficient, b) tip Re number, c) AoA at $r = 0.8R$ and, d) axial induction factor (a) at $r = 0.8R$ as a function of the tip speed ratio. Solid circles on the curves indicate the design TSR of the rotors.

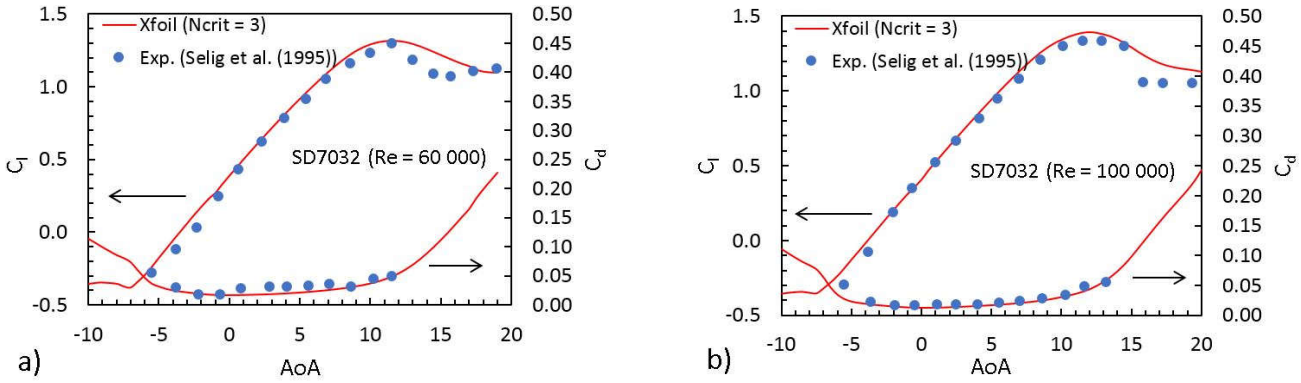

Fig. 9. Comparison of the aerodynamic coefficients of SD7032 predicted by Xfoil with experimental data.

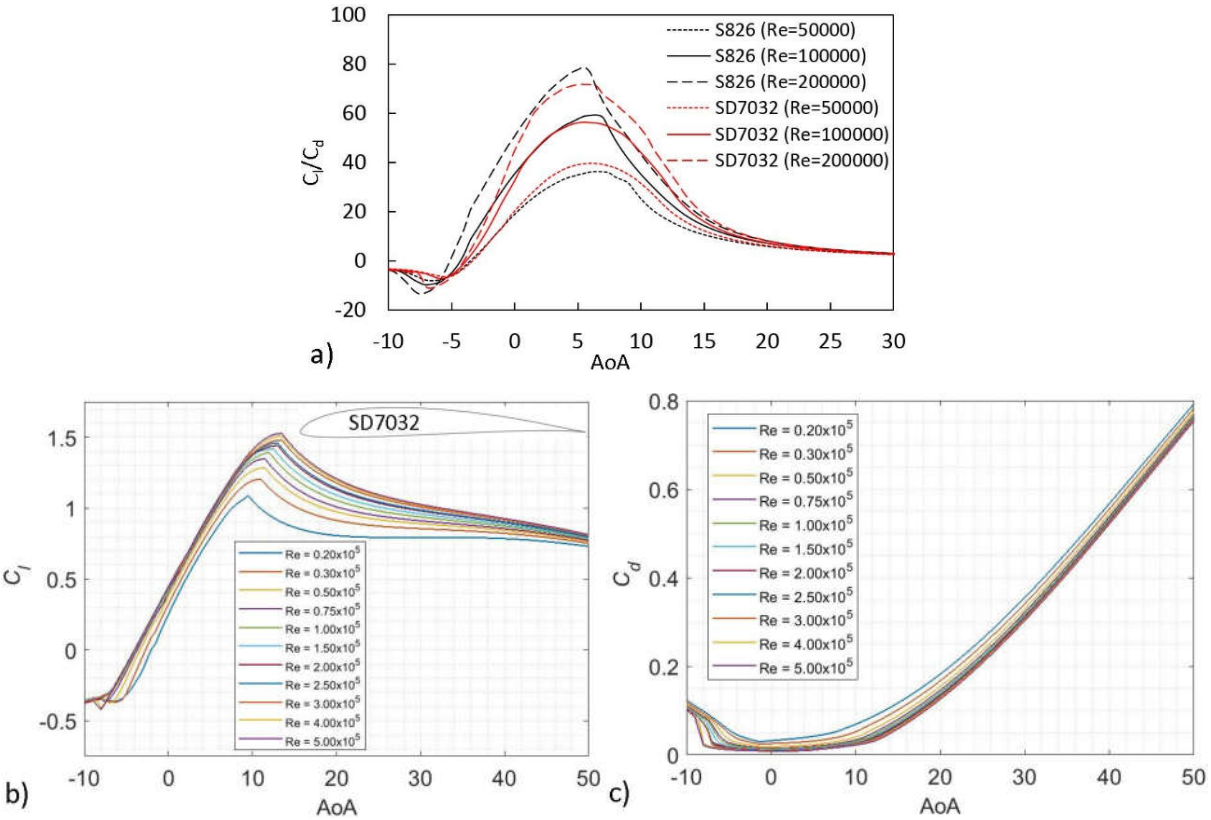

Fig. 10. a) Airfoil efficiency, b) lift, and c) drag coefficients predicted by Xfoil and VC model.

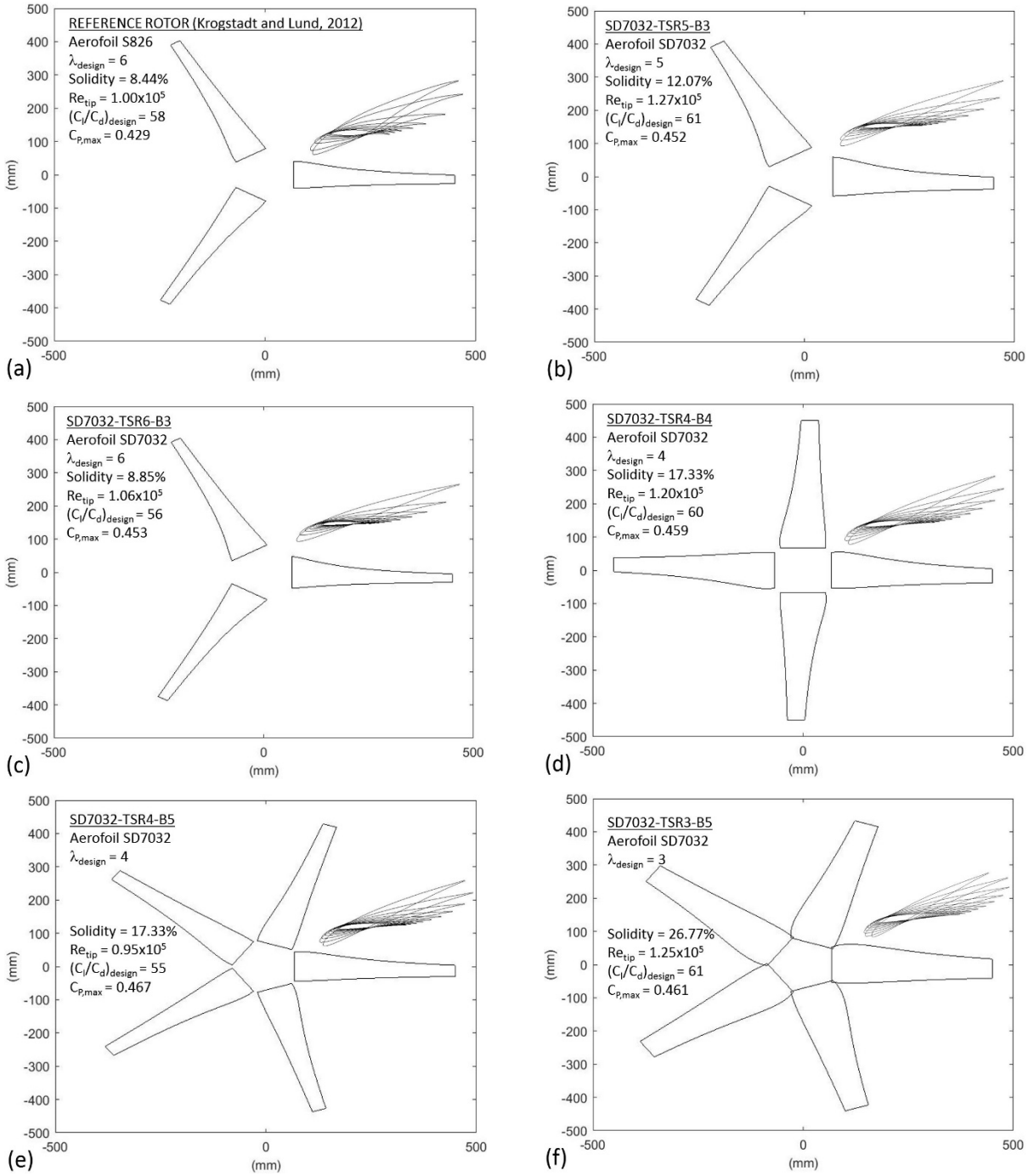

Fig. 11. The Reference Rotor and SD7032 rotors designed.

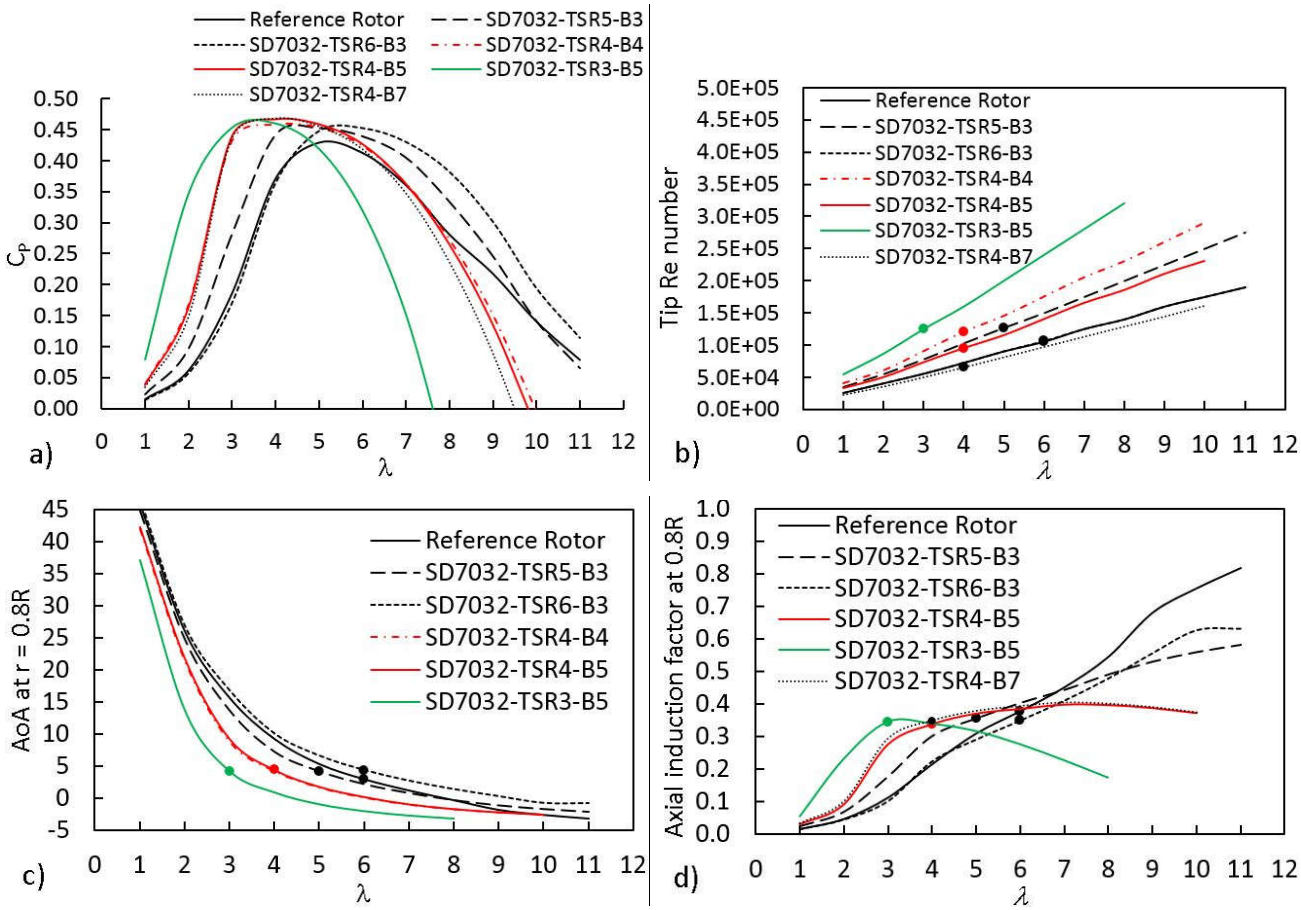

Fig. 12. a) Power coefficient, b) tip Re number, c) AoA at $r = 0.8R$ and, d) axial induction factor (a) at $r = 0.8R$ as a function of the tip speed ratio. Solid circles on the curves indicate the design TSR of the rotors.

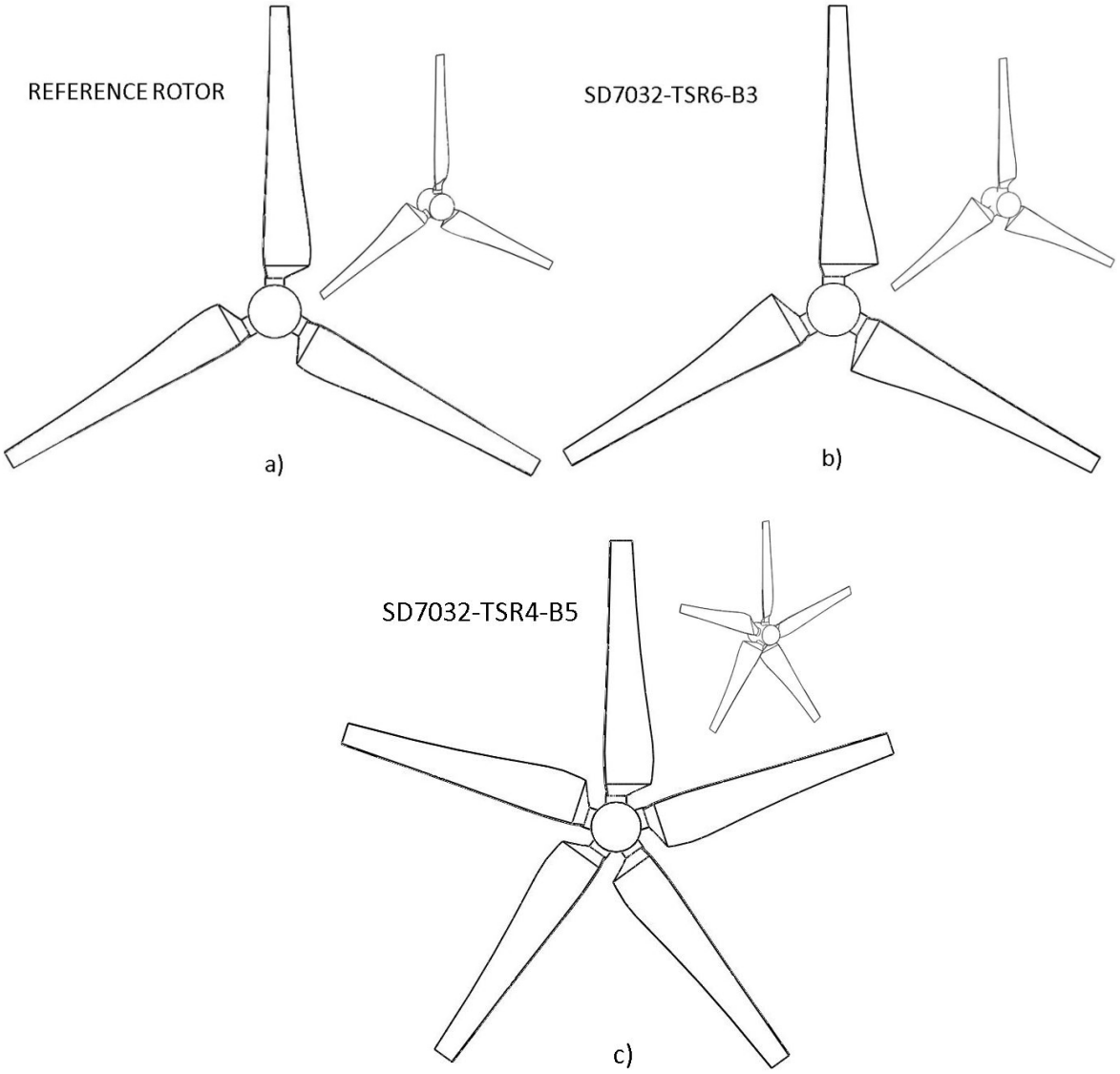

Fig. 13. CAD geometry of selected rotors. Reference Rotor was reproduced from Krogstad and Lund[23].

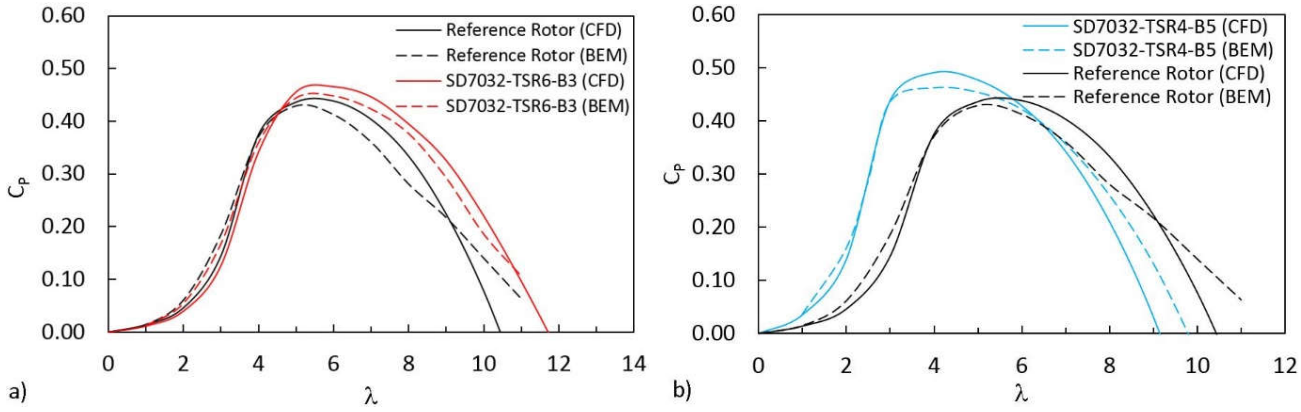

Fig. 14. Comparison of BEM predictions with CFD results a) SD7032-TSR6-B3, and b) SD7032-TSR4-B5.

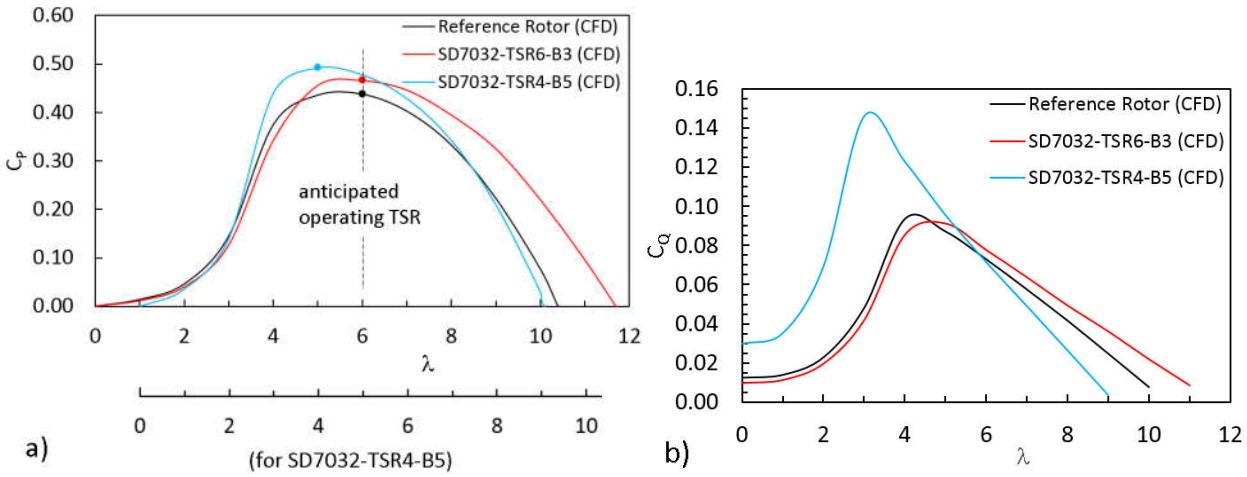

Fig. 15. a) Power coefficients of the rotors (CFD results). SD7032-TSR4-B5's x-axis is shifted one λ to the right. The solid circles on the curves show the design TSR. b) Torque coefficients of the rotors (CFD results).

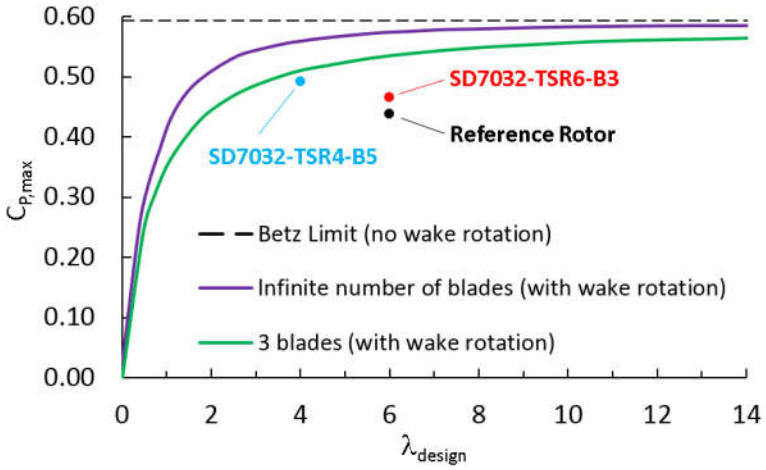

Fig. 16. The three rotors' $C_{P,max}$ predicted by CFD, as well as the theoretical maximum C_P of ideal 3-blade and infinitely many-bladed rotors. C_P curves of ideal rotors are reported in Wilson et al.[59]